

A multiwavelength study of Supernova Remnants in six nearby galaxies.

I: Detection of new X-ray selected Supernova Remnants with Chandra

I.Leonidaki^{1,3}, A.Zezas^{2,4,5} and P.Boumis¹

National Observatory of Athens, Institute of Astronomy and Astrophysics

Harvard-Smithsonian Center for Astrophysics

Astronomical Laboratory, Physics Department, University of Patras

Physics Department, University of Crete

IESL / Foundation for Research and Technology - Hellas

ABSTRACT

We present results from a study of the Supernova Remnant (SNR) population in a sample of six nearby galaxies (NGC 2403, NGC 3077, NGC 4214, NGC 4449, NGC 4395 and NGC 5204) based on *Chandra* archival data. We have detected 244 discrete X-ray sources down to a limiting flux of 10^{-15} erg s⁻¹. We identify 37 X-ray selected thermal SNRs based on their X-ray colors or spectra, 30 of which are new discoveries. In many cases the X-ray classification is confirmed based on counterparts with SNRs identified in other wavelengths. Three of the galaxies in our sample (NGC 4214, NGC 4395 and NGC 5204) are studied for the first time, resulting in the discovery of 13 thermal SNRs. We discuss the properties (luminosity, temperature, density) of the X-ray detected SNRs in the galaxies of our sample in order to address their dependence on their environment. We find that X-ray selected SNRs in irregular galaxies appear to be more luminous than those in spirals. We attribute this to the lower metallicities and therefore more massive progenitor stars of irregular galaxies or the higher local densities of the ISM. We also discuss the X-ray selected SNR populations in the context of the Star Formation Rate of their host galaxies. A comparison of the numbers of observed luminous X-ray selected SNRs with those expected based on the luminosity functions of X-ray SNRs in the MCs and M33 suggest different luminosity distributions between the SNRs in spiral and irregular galaxies with the latter tending to have flatter distributions.

Subject headings: galaxies: individual (NGC 2403, NGC 4214, NGC 4395, NGC 4449, NGC 3077, NGC 5204), X-rays – supernova remnants: X-rays

1. Introduction

Studies of the populations and evolution of Supernova Remnants (SNRs) can provide informa-

tion on the interplay between massive-star formation and the local interstellar medium (ISM; e.g. Chu 1995; Bykov 2005). SNRs provide a significant fraction of the mechanical energy that heats, shapes and chemically enriches the ISM. Therefore, SNRs can be used to investigate global properties of the galaxy's ISM as well as their local environment (Blair & Long 2004). Furthermore, they can be used as proxies to measure the formation of massive stars and can give informa-

¹I.Metaxa and V.Pavlou, Lofos Koufou, Penteli, 15236, Athens, Greece

²60 Garden Street, Cambridge, MA 02138, USA

³26500, Rio, Patra, Greece

⁴P.O Box 2208, GR - 710 03, Heraklion, Crete, Greece

⁵P.O Box 1527, GR - 711 10, Heraklion, Crete, Greece

tion on star formation rate and stellar evolution (Condon & Yin 1990).

Detecting large samples of SNRs in more than one wavebands can provide information about the different processes which take place during their evolution. It is expected that radiation of newly formed SNRs is dominated by the hot material behind the shock-wave producing thermal X-rays (thermal SNRs). One special category are plerion-type SNRs where non-thermal processes are the dominant X-ray emission mechanism (e.g. Safi-Harb et al. 2001; Asaoka & Koyama 1990). Optical filaments are a sign of older SNRs since they form in the cooling regions behind the shock (e.g. Charles & Seward 1995; Stupar & Parker 2009). Emission in radio wavelength is radiated from the vicinity of the shock as well as from the cooling filaments and is easily detectable throughout the life of the remnant (e.g. Dickel 1999; Charles & Seward 1995). In cases where a source is detected in two or more wavebands (e.g. X-rays and optical), it is an indication of material at a wide range of temperatures and the existence of high energy electrons (Charles & Seward 1995). Because of these selection effects, only multiwavelength studies (X-rays, radio, optical, infrared) of large samples of extragalactic SNRs will give a complete image about their nature and evolution as well as their correlation with star-formation.

About 274 SNRs are known to exist in our Galaxy (Green 2009) and a large number of them has been studied in detail. While these studies provide important information on the properties of the individual objects and SNR physics, studies of the population of SNRs are hampered by absorption due to the dust of the Galaxy and distance uncertainties. Therefore, the study of nearby galaxies offers several advantages: the entire galaxy can be studied with fewer observations, SNRs are at the same distance and by selecting higher Galactic latitude, face-on galaxies, internal galactic absorption effects are minimized.

Previous X-ray observations of nearby galaxies ($\lesssim 5$ Mpc) with ROSAT (e.g. Schlegel 1994; Schlegel et al. 2000; Pannuti et al. 2000, 2002; Payne et al. 2004) revealed several X-ray emitting SNRs some of which were also found in other wavebands. These observations showed that SNRs are an important component of the X-ray source populations in galaxies (Blair & Long 1997), es-

pecially at luminosities below 10^{37} erg s $^{-1}$. However, the ROSAT surveys were limited by their low sensitivity and spatial resolution and confined the detection and study of discrete X-ray sources only within our Galaxy and the Local Group. The much better capabilities of *Chandra* in both domains offer a unique opportunity to detect large populations of SNRs in nearby galaxies. The excellent angular resolution of *Chandra* ($\sim 0.5''$) reveals X-ray sources that could not be clearly detected otherwise and allows their identification with sources detected in other wavebands. With typical detection limits of $\sim 10^{37}$ erg s $^{-1}$ in moderate exposures, extragalactic Cas-A or Crab-like SNRs can be detected in nearby galaxies. The capability of *Chandra* to detect X-ray emitting SNRs has been demonstrated in several studies of nearby galaxies; e.g. NGC 1637 – (Immler et al. 2003); NGC 6822 – (Kong et al. 2004); M 31 – (Kong et al. 2002); NGC 2403 – (Schlegel & Pannuti 2003); M 81 – (Swartz et al. 2003).

Even though, about 650, 200 and 50 extragalactic SNRs have been discovered to date in the optical, radio and X-ray bands (e.g. Blair & Long 1997; Matonick & Fesen 1997; Matonick et al. 1997), these numbers come only from a small set of nearby galaxies. Moreover, there is a large gap between detection rates in different bands (less than 50 SNRs have been identified in all three bands) not only due to evolutionary effects but also because of the different observational sensitivity and resolution. In the X-ray band in particular there have not been any systematic studies of the SNR populations in nearby galaxies. Most importantly all studies of X-ray emitting SNRs outside the Local Group have been focused on the identification of X-ray counterparts to SNRs detected in other wavebands, rather than searching for new X-ray emitting SNRs.

This paper is the first in a series undertaking a multiwavelength study of extragalactic SNR populations. We focus on X-ray emitting thermal SNRs rather than plerions because the latter have very similar X-ray spectra to X-ray Binaries (XRBs) and therefore they cannot be identified based on their X-ray properties alone. When possible, we cross-correlate our results with multiwavelength SNR catalogs in order to address the detection efficiency of SNR populations in differ-

ent wavebands.

The outline of this paper is as follows: In §2 we briefly describe each galaxy and prior multiwavelength observations of their SNR populations. In §3 we describe the observations, the data reduction, the analysis techniques used to detect SNR candidates and measurement of their X-ray properties. In §4 we discuss the classification of the X-ray detected SNRs in this study and their correlation with already known X-ray SNRs. Our results are discussed in §5 and finally in §6 we present the conclusions of this work.

2. Sample selection

The sample used for this study consists of six nearby galaxies: NGC 2403, NGC 5204, NGC 4395, NGC 4449, NGC 3077 and NGC 4214. These galaxies are selected from the Third Catalog of Bright Galaxies (RC3; de Vaucouleurs et al. 1995) to be: a) late type ($T > 4$; Hubble type), b) close (≤ 5 Mpc) in order to minimize source confusion (at 5 Mpc, $1'' \simeq 25$ pc), c) at low inclination (≤ 60 degrees) in order to minimize internal extinction and projection effects and d) be above the Galactic plane ($|\text{b}| > 20^\circ$). From this pool of objects we selected galaxies which have *Chandra* archival data with exposure times long enough to achieve a uniform detection limit of 10^{36} erg s^{-1} . We opted to focus on *Chandra* data because of its superior spatial resolution which allows the detection of faint sources in crowded environments. The properties of our sample of galaxies are presented in Table 1.

2.1. Previous surveys of SNR populations in our sample of galaxies

Many of the galaxies in this sample have been extensively studied in several wavelengths. Next we summarize these results and we present any previous X-ray studies of their SNR populations.

NGC 3077: is a member of the gas-rich M81 group, where interaction between M81 and M82 is believed to have triggered starburst activity to both M82 and NGC 3077 (Walter et al. 2002). In a *Chandra* study of NGC 3077, Ott et al. (2003) reported the detection of 3 X-ray sources (S1, S5 and S6) with X-ray characteristics indicative of thermal SNRs. One of these sources (source S1) coincides with a radio source detected by

Rosa-González (2005).

NGC 4214: is a nearby irregular starburst galaxy which features extensive massive star formation throughout its disk. Therefore the existence of SNRs is expected. There is one radio source classified as a radio SNR (source - ϱ of Vukotić et al. 2005) while the nature of sources α and β) (also from the list of Vukotić et al. 2005) is debated (Chomiuk & Wilcots 2009). In addition Chomiuk & Wilcots (2009) find 6 more radio candidate SNRs and 3 sources denoted as SNR/HII. However, no X-ray emitting SNRs have been identified so far in NGC 4214.

NGC 4395: is another irregular starburst galaxy that may host a candidate radio SNR (Sramek 1992; Vukotić et al. 2005) but with no X-ray counterpart. This source is outside the field of view of the observations studied in this work. Up to now, there are no other SNRs identified in NGC 4395 in any wavelength.

NGC 4449: This Magellanic-type irregular, starburst galaxy hosts an extensively studied Cas-A like SNR (e.g. radio: Lacey et al. (2007); optical: Blair et al. (1983); ultraviolet Blair et al. (1984), and X-rays: Patnaude & Fesen (2003)). In addition, Chomiuk & Wilcots (2009) detected 8 candidate SNRs based on radio observations and H α images. In the X-ray band, Summers et al. (2003) report the presence of 2 SNRs and 8 SNR/XRB or SNR/SSS (SSS: Super Soft Source) systems, based on *Chandra* data.

NGC 5204: Three SNRs were optically identified in this irregular galaxy by Matonick & Fesen (1997). Observations for the detection of SNRs in any other waveband have not yet been conducted.

NGC 2403: Matonick et al. (1997) (hereafter MFBL) performed a relatively deep, ground-based, optical search for SNRs in the Scd galaxy NGC 2403. They identified 35 SNRs, two of which were previously known (D’Odorico et al. 1980; Blair et al. 1982). Turner & Ho (1994) classified two radio sources (TH2, TH4) as SNRs, while Eck et al. (2002) detected a radio counterpart (denoted as source μ) to the optically identified SNR MFBL 7. Schlegel & Pannuti (2003) and Pannuti et al. (2007) searched for positional coincidences between their sample of X-ray sources in NGC 2403 and the 35 SNRs of Matonick & Fesen (1997). They found one clear association with

MFBL31 as well as the candidate radio SNR TH2.

In Table 2 we summarize the numbers of optically identified SNRs, radio and already known X-ray SNRs for the galaxies in our sample, emerging from previous studies. Although these studies have presented candidate SNRs, their identification has been based mainly on their multiwavelength associations. Here we present a data analysis focusing on the identification of X-ray selected SNRs based on their thermal X-ray emission.

3. Data Reduction

We have analyzed *Chandra* archival data for the six galaxies in our sample. All exposures were obtained with the back-illuminated Advanced CCD Imaging Spectrometer ACIS-S3 CCD chip (pixel size: $0''.49 \times 0''.49$; energy resolution ~ 120 eV at 1keV; Garmire et al. 2003) at the focal plane of the High Resolution Mirror Assembly (van Speybroeck et al. 1997). The log of the observations is presented in Table 3. We selected observations performed in FAINT Data Mode, full array and exposure times longer than 15 ksec. These parameters provide the largest field-of-view and ensure the detection of sources with X-ray luminosity as low as 10^{36} erg s^{-1} for the most distant galaxy. We found nine datasets for four galaxies of our sample (NGC 2403, NGC 3077, NGC 4214 and NGC 4449) that fulfill the above parameters. In the case of NGC 4395, three observations were available, fulfilling the FAINT Data Mode and exposure time criteria. Two out of the three were performed in 1/8 subarray mode while the third one was performed in custom subarray mode. We used only the third observation which covers a large area of the galaxy ($\sim 30\%$ of its D_{25}). As for NGC 5204, observations are performed in 1/8 subarray mode. Of these, 12 have short (~ 5 ksec) exposures and only one has a longer 15 ksec exposure, which fulfills our exposure threshold. However, the 12 5ksec exposures are taken with different roll angles. Since each of them fulfill our 10^{36} erg s^{-1} limiting luminosity requirement and their combination covers $\sim 80\%$ of the D_{25} area of the galaxy, we opted to use them in our study.

The data analysis was performed with the CIAO tool suite version 3.4 and CALDB version 3.3.0, unless otherwise stated. Each dataset was

analyzed following the *Chandra* Standard Data Processing threads (SDP)¹.

Since we are interested in multi-wavelength comparison of the X-ray sources, application of astrometric correction is a critical element of this study. We searched for counterparts of point-like, bright X-ray sources (> 100 counts) in the 2MASS All Sky Catalog of point sources (Cutri et al. 2003). We found typically 3-5 counterparts for each galaxy. The comparison between the coordinates of the X-ray sources and the 2MASS counterparts yielded offsets $< 0.5''$ consistent with the average astrometric error of the *Chandra* Pointing². We applied these offsets to the event files. Then, we reprocessed them to apply corrections for gain and Charge Transfer Inefficiency (CTI). We searched over source free regions for background flares by creating lightcurves with a time resolution of 200 sec. We applied a sigma-clipping algorithm³ on the lightcurves in order to identify time periods of anomalous background levels ($\pm 3\sigma$ from the mean value). No significant flaring of the background was observed in any of the datasets.

3.1. Imaging Analysis

After the initial processing of the data, we created images in four energy bands: soft (S: 0.3 - 1.0 keV), medium (M: 1.0 - 2.5 keV), hard (H: 2.5 - 7.0 keV) and total (T: 0.3 - 7.0 keV). In the case of multiple observations of an object, we aligned each event file of a given observation to a chosen reference event file. We then reprojected and merged the events of each band (S, M, H, T) for each dataset using the CIAO script *mergeall*.

We set the upper energy limit of the medium band to 2.5 keV because energies up to that value include emission lines from hot thermal plasma and are influenced by photoelectric absorption of the column densities typically seen in galaxies. These emission lines are of great importance to investigate since they allow us to distinguish between low temperature thermal emitting gas and harder emission from a power-law or hotter thermal continuum. The goal of this study is the identification of X-ray emitting SNRs and our first

¹See <http://asc.harvard.edu/ciao/threads>.

²See <http://cxc.harvard.edu/cal/ASPECT/celmon/>

³See http://cxc.harvard.edu/ciao3.4/ahelp/analyze_ltrcv.html.

classification criterion is based on the Soft X-ray color: $\text{Col1} = \log(S/M)$, where S, M are the counts in the soft and medium bands. Therefore, we defined the energy range of the soft and medium bands in a way that provides the maximum separation of the S/M color distribution, for the optically thin, soft thermal plasma models characteristic of thermal SNRs ($kT \sim 0.5 - 1.5$ keV). We identified these bands by estimating the expected number of counts in different energy bands in a typical observation of our galaxies, assuming an *apec* (Smith et al. 2001) thermal plasma model of different temperatures. The transition between the soft and medium band was in the 0.5 - 1.5 keV range since in this range the peak and strength of the FeL blend, which is characteristic of thermal plasma of this temperature, shows the strongest variation.

In Fig. 1 we show the S/M color for four different choices of the two bands: S_1 : 0.3 - 0.5 keV and M_1 : 0.5 - 2.5 keV, S_2 : 0.3 - 0.7 keV and M_2 : 0.7 - 2.5 keV, S_3 : 0.3 - 1.0 keV and M_3 : 1.0 - 2.5 keV, S_4 : 0.3 - 1.5 keV and M_4 : 1.5 - 2.5 keV. The different points show the S/M color which corresponds to different choices of temperature (0.25 - 2.0 keV from the bottom towards the top points of each set). As we can see from this figure, the third and fourth band selections (S_3 : 0.3 - 1.0 keV and M_3 : 1.0 - 2.5 keV, S_4 : 0.3 - 1.5 keV and M_4 : 1.5 - 2.5 keV) give the maximum discrimination of the S/M color for the different temperatures of a thermal model. Since these particular band selections do not show any major differences, we chose the third one (S_3 : 0.3 - 1.0 keV and M_3 : 1.0 - 2.5 keV; circles in Fig. 1) in order to ensure a larger number of counts in the medium band. Regarding the other energy bands, the combination of the medium and the hard band (2.5 - 7.0 keV) gives a good representation of the continuum emission and temperature while the total band (0.3 - 7.0 keV) is very useful for measuring the total flux of a source especially in the case of a small number of counts (e.g. Zezas et al. 2006).

In order to directly compare the intensity and spectra of sources detected by different instruments or observations, we accounted for variations of the ACIS sensitivity by creating exposure maps for each data set in the four bands (S, M, H and T). The CIAO 3.4 suite and CALDB 3.3.0 allow us to include in the exposure maps the time-dependent

spatial variations of the ACIS sensitivity due to the contaminant on the detector window. Each energy's band exposure map is the sum of sub-bands (monochromatic maps), weighted only for the differences in the bandwidth. This is equivalent to a flat energy spectrum ($\Gamma=0$, $N_H=0$) or estimating the integral of the effective area over each broad band (see Zezas et al. 2006). In the case of single observations we used the CIAO tool *mkeexpmap*.

We note that because *mergeall* for a multiple-chip, multiple observation exposure map was not able to extract merged exposure maps or use correctly the *asol* files of the multiple exposures, we used the same script for extracting exposure maps for each band and each observation and then combined them with the CIAO tool *dmimgcalc*.

3.2. Source Detection

We searched each dataset for sources in the four energy bands, using the *wavdetect* tool of CIAO⁴. The significance threshold was set to one false detection over the searched area while the scales parameter was set to 2.0, 4.0, 8.0 and 16.0 pixels. We used the relevant exposure maps in order to avoid the detection of spurious sources close to the CCD edges. The results of the *wavdetect* run for each band and for each exposure were cross-correlated and combined to create one source list for each galaxy, covering the D_{25} ⁵ ellipse of the galaxy. In the case of multiple observations, the detection was performed on the co-added images, in order to achieve the maximum sensitivity.

We detected a total of 244 discrete X-ray sources in our sample of six galaxies (22 in NGC 3077, 16 in NGC 4395, 26 in NGC 4449, 44 in NGC 4214, 125 in NGC 2403 and 11 in NGC 5204) down to a limiting flux of 10^{-15} erg $\text{cm}^{-2}\text{s}^{-1}$ in the 0.3 - 10.0 keV band.

We calculated the expected number of background sources for each galaxy in our sample based on the *Chandra* Multiwavelength Project (ChaMP) X-ray point source catalog and the cumulative luminosity distribution of Kim et al. (2007). Given that the investigated sources of this

⁴See <http://asc.harvard.edu/ciao/threads/wavdetect>.

⁵The D_{25} ellipse is defined as the optical isophote at the B-band surface brightness of 25 mag arcsec^{-2} (e.g. RC3, de Vaucouleurs et al. 1995).

study are predominantly soft sources, we used the 0.5 - 2.0 keV $\log N - \log S$ in order to estimate the number of background sources down to our limiting flux of 10^{-15} erg s $^{-1}$ cm $^{-2}$ within the area of each galaxy covered by the *Chandra* observations. The number of expected background sources is given in Table 4.

3.3. Photometry

In order to perform photometry of the detected X-ray sources, we defined source apertures on the total band image, while ensuring that i) they do not encompass other neighbouring sources or significant diffuse emission and ii) they cover at least 90% of the encircled energy of the source's Point Spread Function (PSF) at a given off-axis angle and a typical energy of 1.4 keV (appropriate for the soft sources we investigate in this work). The typical radius of these apertures is $\sim 1.0'' - 1.5''$. The background for each source was measured locally from apertures defined to cover a large area around them, while ensuring that the diffuse emission does not vary significantly over the background area. We measured the number of raw counts for each source and its corresponding background in each of the S, M, H and T bands, using the *dmextract* tool of CIAO⁶. To account for exposure variations across the ACIS-S3 CCD area, we calculated corrections of the effective area for each source by normalising the exposure maps of each band with respect to a reference point close to the center of each galaxy such as to minimize variations of the sensitivity over the studied area (see Zezas et al. 2006). In the case of multiple exposures, the reference point was chosen on one of the merged exposure maps. This way we also correct for sensitivity variations between different observations. In Tables 5-10 we present the observed (raw) source and background counts in the S, M, H and T bands for sources that appear to be potential SNRs (see §3.4.1) and sources with very strong soft components based on their X-ray colors. We also present the background/source area ratio (which is common in all energy bands since the same source and background apertures were used) as well as the background/source effective area ratio in the soft energy band.

⁶See <http://asc.harvard.edu/ciao/threads/dmextract>.

3.4. Spectral analysis

3.4.1. X-ray colors

Since our goal is to identify candidate sources with soft thermal spectra ($kT \leq 2$ keV, typical of thermal SNRs; Schlegel 1994), initially we use the X-ray photometry derived in the previous section. Instead of hardness ratios which have less symmetric posterior probabilities (Park et al. 2006), we calculated X-ray colors defined as $C1 = \log(S/M)$, $C2 = \log(M/H)$ and $C3 = \log(S/H)$, where S, M, H are the net counts in the Soft (0.3 - 1.0 keV), Medium (1.0 - 2.5 keV) and Hard (2.5 - 7.0 keV) band, respectively. The X-ray colors can be used to obtain information on the spectral properties of the X-ray emission even in the case of small number of counts when spectral fitting is not possible.

In the small number of counts regime where most of our sources belong, the Poisson distribution becomes distinctly asymmetric. In this case it is more appropriate to use a method based on the Bayesian estimate of the "real" source intensity which takes into account the Poisson nature of the probability distributions for the source counts as well as the effective exposure at the position of the source (van Dyk et al. 2001; Park et al. 2006). Furthermore, in the case of non-detections in one or more bands this method can also provide upper limits on the X-ray colors. Since the numerical integration of the Bayesian method is more accurate but computationally more intensive, we used it for sources with fewer than 70 counts in any of the soft, medium or hard bands. The integration was performed using the Gaussian quadrature algorithm with 2500 bins. For sources with more than 70 counts, we used the Gibbs algorithm with 10^5 draws, 15000 of which were rejected as burn-in draws. In both cases the confidence level was set at 68.0%.

In Figs. 2-7 we plot the C1 against C2 X-ray colors for the detected X-ray sources. On the same plots we added grids for power-law and thermal plasma models for different values of temperature (kT), absorbing H I column density (N_H) and photon index Γ . Sources that appear to have temperatures below 2 keV and mainly lie on the thermal grid (locus of SNRs) as well as those which are consistent with the thermal grid within their error-bars, are potential SNRs. In the case of plerion SNRs, we expect them to lie on the power-law

grid as their X-ray emission is non-thermal with photon indices of 1.7–2.0 (e.g. Asaoka & Koyama 1990). Since their spectra are very similar to those of X-ray binaries, they cannot be selected solely on the basis of their X-ray properties. In Tables 11-16 we present the calculated X-ray colors (C1, C2 and C3) for potential SNRs in all galaxies of our sample as well as for the soft sources that lie on the right corner of the plots which indicate an extra soft component due to diffuse emission. For comparison, we show which sources have extracted spectra (see §3.4.2) and the suggested classification based on their spectroscopy (see §4).

3.4.2. Spectral fitting

We tested the X-ray color tentative classification of thermal SNRs by performing spectral analysis for sources with adequate number of counts. We also examined the soft sources on the bottom right corner of the color-color plots. We extracted PI spectra, auxiliary response files and redistribution matrix files with the *specextract CIAO* script which takes into account spatial variations of the effective area by creating the weighted redistribution matrix files and auxiliary response files (wrmf, warf) for each source. Spectral fit was performed with XSPEC version 11. The upgraded 3.4.2 version of CALDB was used.

For sources with more than 50 counts, χ^2 statistics were used. The spectral channels were binned for the spectral fitting analysis in order to contain at least up to 25 counts per bin before background subtraction for sources with high background (source counts with $> 5\%$ contamination from background counts) and 15 counts for sources with low background ($< 5\%$ contamination from background counts). This ensures that in either case we have between at least 10 counts after background subtraction in each bin. The corresponding background was subtracted from the source spectrum during the fitting process. For sources with few counts ($\lesssim 50$) the Cash maximum likelihood statistic was used (Cash 1979), which is more appropriate than χ^2 statistics in the case of small number of counts. The spectra were not binned in order to preserve the maximum amount of information for statistical analysis.

Each spectrum was initially fitted separately with two different models: power-law (PL) and thermal plasma (apec; Smith et al. 2001). We

opted to use the apec model since it is the most up to date optically thin equilibrium thermal plasma model including significant improvements in the number of spectral lines and their oscillator strengths. In a few cases where we had indication for abnormally strong emission lines, indicative for a non-equilibrium plasma, we also used the nei model (e.g. source LZB15 in NGC 3077). Also sources well-fitted with an apec model but presented unrealistically low temperatures for a thermal plasma (< 0.1 keV), were re-fitted with a blackbody (bbody) model.

The models were coupled with a photoelectric absorption model (phabs) due to the Galactic Interstellar Medium as well as to the material within each galaxy, with the restriction that the derived column densities should exceed the weighted average Galactic line-of-sight values obtained from the LAB (Leiden/Argentine/Bonn) Survey (Kalberla et al. 2005) of Galactic H I ⁷. We also assumed solar metallicities for all galaxies since the quality of the data did not allow us to constrain the abundance.

In some cases (e.g. LZB4 and LZB5 in NGC 4449; LZB24 in NGC 4214; LZB64, LZB99 and LZB101 in NGC 2403; LZB11 in NGC5204) the single component models gave either unacceptable fits ($\chi^2 > 2$), strong line-like residuals or unrealistic best fit parameters. In this case we fitted the data with a two-component (PL + apec) model with the same absorption. As discussed in Protassov & van Dyk (2002), the use of the F-test in order to assess the improvement of the fit in this case is not statistically proper.

We selected the best model for each source based on the quality of the fit (e.g. good statistical fit mainly determined by $\chi_\nu^2 \sim 1$ for chi-square statistics, and goodness-of-fit $\sim 50\%$ for Cash statistics) and the plausibility of the parameter values (thermal component temperature ≤ 3 keV, power law photon index ≤ 4). In the case of multiple observations, we fitted the individual spectra simultaneously with the same model. All model parameters apart from the normalization were determined by the first dataset.

The best fits obtained for potential SNRs (sources in the locus of SNRs as well as those in the bottom right corner of the color-color plots)

⁷See <http://heasarc.nasa.gov/cgi-bin/Tools/w3nh/w3nh.pl>

in each galaxy are summarized in Tables 17-22. Column 1 presents the source ID as well as the observation ID in the case of multiple exposures. For the latter, we used only observations at which the corresponding source is detected with adequate number of counts and does not lie near the borders of the CCD (~ 100 pixels away). Column 2 shows the fitted model. Column 3 gives the HI column density obtained from fitting the phabs (photoelectric absorption) component and Column 4 gives the best fit photon index for the power-law model or the temperature for the apec or black body models. Column 5 presents the model normalization. In the case of multiple exposures, we give the multiplicative factor for the intensity of the different spectra that were fitted simultaneously, with respect to the first observation of each source. All uncertainties at the 90% confidence level are calculated with the *error* command of XSPEC. Columns 6 and 7 present the absorbed and unabsorbed flux in the 0.3-10.0 keV energy band. Although spectroscopy is derived from the 0.3-7.0 keV energy band, we chose to calculate the fluxes in the 0.3-10.0 keV energy band for consistency with previous X-ray publications. Column 8 is the source classification based on the X-ray spectral fits: the presence of only low temperature thermal component(s) in a fit strongly indicates that the source is an SNR while sources having hard components (power-law) to their spectra are most likely XRBs. Sources well-fitted with a low-temperature (~ 100 eV) black body model are denoted as Super Soft Sources (SSS).

We mention that there are cases of SNRs (e.g. LZB15 in NGC 3077) where the electron temperature of the best-fit thermal model is relatively high (> 2 keV). This may imply a non-equilibrium state of the collisionally ionized plasma of the source (these sources are also well-fitted with a nei model). However, this is not an unusual phenomenon. Kong et al. (2004) propose that non-equilibrium state of the collisionally ionized plasma could either come from the shock-heated swept-up circumstellar medium or it is due to inhomogeneity of the ISM.

What is more, there are sources with a small number of counts that are fitted with high values of column density. There is a well known positive correlation between the normalization of a model

and the absorbing column density. Therefore, in the case of low number of counts spectra (such as those we consider here) it is possible that we can obtain high best-fit HI column densities and hence high inferred unabsorbed source luminosities (resulting from the high normalization of the low-energy source spectral components).

4. SNR classification and correlations with already detected X-ray SNRs

On the basis of these results, we divide our X-ray detected SNRs into three types: a) SNRs, b) probable SNRs, and c) candidate SNRs. As SNRs we consider point-like non-variable sources which have spectra consistent with a single or two-component low temperature thermal X-ray spectrum ($kT < 3$ keV). We consider as probable SNRs sources which: i) fulfill the above criteria but have a small number of counts (< 50) and/or large errors on their spectral parameters and/or ii) vary by $< 15\%$ in flux between different observations. Candidate SNRs are sources for which it was not possible to extract any X-ray spectra but fulfill the hardness ratio criteria (i.e. they lie, within their error bars, on the low-temperature part of the thermal grid of the color-color plot). Sources for which we cannot distinguish between a thermal and a non-thermal model are denoted as unclassified. Nonetheless, their spectral parameters are also presented in the relevant tables.

We find good agreement between the spectral parameters derived from the X-ray colors and the analysis of the X-ray spectra, giving us confidence in the use of hardness ratio diagrams as a diagnostic tool for the initial identification of thermal SNRs. We note that all sources considered in this study are pointlike (physical scales 5 and 11 pc for the closest and more distant galaxies respectively) limiting the possibility that they are local enhancements of the general diffuse X-ray components.

A total of 37 X-ray selected SNRs (8 SNRs, 24 probable SNRs and 5 candidate SNRs) are detected in this study, 30 of which are new identifications. One third of these new sources have been also identified as SNRs based on other multi-wavelength observations, giving us confidence that the X-ray selection scheme is robust. We are in the process of analysing additional deeper multi-

wavelength data in order to extend the classification to other objects (Leonidaki et al. in preparation). Three of the galaxies in our sample (NGC 4214, NGC 5204 and NGC 4395) containing 71 X-ray detected sources are studied for the first time in this context, and they exhibit 12 new X-ray SNRs. There is one additional source in NGC 3077 which appears to be in the data after visual inspection of the raw and smoothed images. This source seems to be extended and in a location with significant diffuse emission, and is not detected by wavedetect. The same source was also included in the source list of Ott et al. (2003) only after visual inspection of the data (source 5, classified as SNR). Since it could be a local enhancement of diffuse emission and for that reason has not been detected by a robust blind search algorithm like wavedetect, we opted not to include it in our source list. No other X-ray known SNRs have not been detected by this study.

In the case of two sources in NGC 4449 our results suggest slightly different classifications than those published in previous studies (e.g. Summers et al. 2003). We classify source LZB4 as an XRB based on its relatively hard spectrum ($\Gamma=2.3$). Source LZB26 can be fitted equally well with an absorbed apec ($kT\sim 1.02$ keV) or an absorbed black body ($kT\sim 0.2$ keV). Therefore we consider it as a probable SNR.

The requirement that the sources we consider as SNRs are non-variable minimizes the possibility that they are super-soft or quasi-soft X-ray sources. Furthermore, super-soft sources typically have much softer spectra ($kT \leq 0.1$ keV), while quasi-soft sources have soft spectra with a power-law component (e.g. Greiner 1996; Di Stefano & Kong 2004). Our SNRs instead have typically “clean” thermal spectra. Additionally, one third of our X-ray SNR identification are confirmed based on known SNRs in other wavelengths, giving us confidence on these selection criteria. We cross-correlated all X-ray selected SNRs against the 2MASS catalog and checked their optical counterparts on SDSS images. We found only one source (LZB22 in NGC4449) that coincides with a foreground star.

Furthermore, the soft thermal spectra ($kT \leq 2$ keV) of the detected SNRs minimize the possibility that they are background sources such as AGNs or QSOs. The latter exhibit harder X-ray

spectra with photon indices $\Gamma \leq 2 - 2.5$, added as such they would have been excluded in our selection process.

We also cross-correlated all X-ray selected SNRs against the 2MASS catalog and checked their optical counterparts on SDSS images. Only one source (LZB22 in NGC4449) coincides with a foreground star. This source is not included in the SNR sample of the relevant galaxy.

5. Discussion

5.1. Multiwavelength associations

Comparison of the emission of SNRs in different wavebands can provide information about the evolutionary stage of the sources and/or can illustrate selection effects. For that reason we searched for coincidences between the X-ray identified SNRs (see §4) with SNRs in optical and radio wavebands (see §3). In Fig. 8 we present the overlap between X-ray, optical and radio selected SNRs, in the form of Venn diagrams for all galaxies in our sample, except for NGC 5204 where no X-ray SNRs were identified. The X-ray sources we consider in this comparison are denoted as SNRs or probable SNRs. All multi-wavelength comparisons were performed for the same area for each galaxy. For that reason we excluded the radio SNR in NGC 4395 (Vukotić et al. 2005) as it is outside the *Chandra* field of view. In addition, we excluded the radio candidate SNRs α and β in NGC 4214 (Vukotić et al. 2005) the nature of which is debated (Chomiuk & Wilcots 2009). In this comparison, we consider only radio candidate SNRs, excluding SNR/HII composite objects from Chomiuk & Wilcots (2009) which present spectral index consistent either with an HII region or SNR.

From the 36 optically identified SNRs (mainly on the basis of narrow-band photometry) 8 possess X-ray counterparts (corresponding to a detection rate of 22%), while 7 out of the 19 radio-candidate SNRs have X-ray counterparts (detection rate of 37%). Little overlap appears to be between optical and radio SNRs ($\sim 6\%$). In the case of NGC 2403 (Fig. 9) we find a larger number of X-ray SNRs than reported in the study of Pannuti et al. (2007). This is due to: (a) the much longer exposures used in the present study, and (b) the different selection criteria (Pannuti et al. 2007 focused on optically/radio selected samples

of X-ray emitting SNRs).

The detection rate of SNRs in different wavebands strongly depends on the properties of the surrounding medium of the source. For example, Pannuti et al. (2007) point out that optical searches are more likely to detect SNRs located in regions of low diffuse emission, while radio and X-ray searches are more likely to detect SNRs in regions of high optical confusion. In this study, the sample of radio SNRs is limited by the lack of deep radio surveys for SNRs for half of our galaxies. This could contribute to the difference in the detection rates between optical/X-ray SNRs and optical/radio, X-ray/radio SNRs.

5.1.1. *Supernova Remnants or X-ray Binaries?*

Three X-ray sources (LZB93, LZB99, LZB104) in NGC 2403, although spectroscopically identified as XRBs on the basis of their hard X-ray emission (and with X-ray luminosities consistent with those of XRBs, see Table 23), are associated with optically known SNRs in the catalog of Matonick et al. (1997). This is also the case for the spectroscopically identified XRB (LZB26) in NGC 4214 which coincides with a radio SNR/HII source detected by Chomiuk & Wilcots (2009) (see Table 23). One possible interpretation is that of an X-ray binary coincident with a supernova remnant, possibly associated with the supernova that produced the compact object in the binary. In this case the SNR is responsible for the observed optical and radio emission while the binary system produces the X-ray emission. The X-ray luminosity of active XRBs ($\geq 10^{37}$ erg s $^{-1}$) is higher than that of SNRs (typically $10^{35} - 10^{37}$ erg s $^{-1}$) and therefore they can overshadow the latter. The exemplar of this type of objects is the SS 433/W50 SNR/XRB system (e.g. Safi-Harb & Petre 1999), while a few other candidates have been identified in other galaxies on the basis of hard and/or variable X-ray sources associated with optically or radio identified SNRs (Pannuti et al. 2007).

We searched for additional sources of this class witnessed by composite thermal – non-thermal spectra (point-like sources requiring power-law and apec spectral components) where the thermal component dominates, indicating that they could be SNR/XRB systems. Four X-ray detected sources in our sample of galaxies (LZB4 in NGC 4449, LZB24 in NGC 4214 and LZB64, LZB101

in NGC2403) are fitted with composite thermal – non-thermal spectra. The thermal component contributes $< 30\%$ to the total X-ray emission of these systems therefore their classification as XRBs is more robust.

5.2. $N_H - L_X, kT - L_X$

We examine the HI column density (N_H) of the X-ray selected SNRs as a proxy of the density of their local ISM. SNRs in dense star-forming regions are usually associated with significant amounts of cold gas, which could result in excess absorption towards their line-of-sight. Simulations of SNRs embedded in dense environments show that they tend to have higher luminosities (e.g Chevalier & Fransson 2001). Therefore, one would expect a correlation between their luminosity and the density of their environment. In Fig.10 we plot the column density against the absorption-corrected luminosity of the spectroscopically identified SNRs in this study, based on their best fit parameters (Tables 17-22). The Galactic column density value has been subtracted from the measured N_H value. The error bars correspond to the 90% confidence level for one interesting parameter. In this plot we do not include sources with N_H value pegged on the Galactic value. Non-existence of down-side N_H or left-side luminosity error bars indicates upper bounds at the 90% confidence level. In the same plots we also show for comparison a sample of Magellanic Cloud (MC) SNRs from the *Chandra* Supernova Remnants Catalogue⁸. From that plot we see that our sample of extragalactic SNRs have systematically higher X-ray luminosities than the MC-SNRs and that there is not a trend between HI column density and luminosity. This could indicate that the contribution of the local environment to the overall HI column density is very smaller, or that the local densities are not high enough to significantly affect the X-ray luminosity.

In Fig. 11 we investigate the correlation between SNR temperature and absorption-corrected luminosity. The majority of our SNRs have temperatures in the 0.1–1.0 keV range, typical for thermal SNRs (e.g. Schlegel 1994) and luminosities in the 5×10^{36} to 5×10^{39} erg s $^{-1}$ range. We do not see any significant correlation be-

⁸See <http://hea-www.cfa.harvard.edu/ChandraSNR/>

tween luminosity and temperature. However, we do see a population of SNRs with high temperatures or high luminosities. As discussed in §3.4.2 the objects with high temperatures indicate sources with non-equilibrium spectra while the high absorption-corrected luminosities of few objects are probably artifact of their large (and often poorly constrained) column density. In fact often the luminosities of these objects are consistent with the main population of SNRs within their errorbars. The dashed line indicates the expected relation between the unabsorbed X-ray luminosity and temperature for a thermal source at a distance of 5 Mpc, based on an apec model with fixed emission measure (EM). From this model we see a weak dependence of the X-ray luminosity to temperature if it is below 1 keV. We note that in the case of double thermal models (apec+apec), the higher value temperature was used.

5.3. SNRs and Star Formation Rate (SFR)

Since core-collapse SNRs are the endpoints of the evolution of the most massive stars, they are good indicators of the current SFR. Although there are several calibrations of the radio SNR rate - SFR (e.g. Condon & Yin 1990), the investigation of the X-ray SNR rate with SFR are hampered due to the lack of large and secure samples of X-ray selected SNRs. Here we attempt to derive such a calibration using the uniform samples of X-ray SNRs selected in §4.

All galaxies in our sample have accurate measurements of their integrated FIR luminosity (Ho et al. 1997, Table 25), so we opted to use this as a SFR proxy. The FIR luminosity is based on integrated flux measurements with IRAS in the 60 and 100 μm bands which were used to calculate the 42–122 μm broad-band FIR luminosity using the calibration of Rice et al. (1988); Helou et al. (1988) and the distances in Table 1. We are aware that the FIR luminosity tends to overestimate the instantaneous SFR since it includes contribution from late type stars, however for the purpose of the comparison of the SNR rate with the SFR in this set of galaxies it is better suited than the $\text{H}\alpha$ luminosity which is heavily affected by extinction.

5.3.1. X-ray properties of SNRs and Star Formation

In order to investigate the X-ray properties of SNRs in different star-forming environments, we calculate the average integrated 0.3 - 10.0 keV unabsorbed X-ray luminosity of SNRs detected down to a luminosity of 5×10^{36} erg s⁻¹ for each galaxy. This limiting luminosity is based on a preliminary analysis of the luminosity distribution of the SNRs in our sample (Leonidaki et al. in preparation) which shows that the sample of SNRs is complete down to this limit. We only consider sources classified as SNRs or probable SNRs by this study. We also include in our sample the X-ray detected SNRs (above our detection limit) in three more galaxies from the work of Pannuti et al. (2007). The 0.2-10.0 keV average unabsorbed X-ray luminosity of the SNRs in Pannuti et al. were converted to the 0.3-10.0 keV energy range assuming a thermal bremsstrahlung model with a temperature of $kT = 0.5$ keV. Although the 0.1 keV difference in the energy bands has only a small effect ($\sim 6.5\%$) on the unabsorbed X-ray luminosity for a typical SNR spectrum, we performed the conversion for consistency.

In Fig. 12 we plot the average unabsorbed X-ray luminosities of SNRs in spiral galaxies (squares) and irregular galaxies (triangles) from our sample against the integrated 42–122 μm FIR luminosity of each galaxy which is a good star-formation rate indicator. In the same plot we include the SNRs with luminosity greater than 5×10^{36} erg s⁻¹ SNRs (circles) from the LMC and SMC (*Chandra* Supernova Remnants Catalogue).

As expected, we do not see any correlation between the average SNR X-ray luminosity and the total FIR luminosity of their host galaxy. However, we do see a systematic trend for more luminous SNRs to be associated with irregular galaxies. This indicates a difference of the SNR population characteristics between the two samples. This could be due to the typically lower metallicity of irregular galaxies than in typical spiral galaxies (e.g. Pagel & Edmunds 1981; Garnett 2002). Low abundances result in weaker stellar winds (e.g. Lamers & Cassinelli 1999) which in turn produce higher mass supernova progenitors. More massive progenitors are expected to produce more massive ejecta and stronger shocks which would lead to

higher SNR X-ray luminosities.

Other possible interpretations include the non-uniform ISM which is often the case in irregular galaxies, or possible Initial Mass Function (IMF) differences between spiral and irregular galaxies. In the first case local enhancements of the ISM (especially at the star forming regions) could result to more luminous SNRs, while in the second case, flatter or top heavy IMFs which in some instances have been proposed for irregular galaxies, would result to larger number of SNe with more massive progenitors.

5.3.2. Number of SNRs and SFR

Since SNRs are the short-lived end-points of young stars we would expect a linear relation between the number of X-ray selected SNRs and SFR (e.g. Condon & Yin 1990). To verify this connection, we plot the number of SNRs above the completeness limit of our sample (5×10^{36}) against the integrated FIR luminosity of each galaxy (Fig. 13). For comparison, in the same plot we include the X-ray selected sample of SNRs in the MCs from the XMM-Newton study of Ghavamian et al. (2005). Although in the case of SMC this study covers a fraction of the area of the galaxy, a comparison with the ASCA-selected SNR sample of Yokogawa et al. (2000) which covers almost the whole galaxy show that the sample of Ghavamian et al. is complete, and the MC SNR census extends down to a luminosity of 10^{35} erg s⁻¹, much lower than our completeness threshold.

In order to compare the Magellanic Cloud SNR populations with our sample, we use the luminosity distributions of the MCs SNRs from Ghavamian et al. (2005) and rescale their observed numbers to the numbers of SNRs down to our limiting luminosity of 5×10^{36} erg s⁻¹, assuming a cumulative slope of -0.5 (see Table 24), which is a good representation of the MC SNR populations. We did not use the SNRs in the three galaxies of Pannuti et al. since the different selection criteria of the two studies (optically selected X-ray emitting SNRs in the study of Pannuti et al. versus X-ray selected SNRs in this study) do not allow a direct comparison of the two populations.

We find a linear relation between the number of X-ray selected SNRs and the FIR luminosity (Fig.

13), but the small number of objects does not allow us to quantify their scaling relation. However, a linear correlation coefficient of 0.72 shows that this is a significant correlation. Even if we remove NGC 2403, which seems to drive the correlation, or NGC 4449 which has the greatest distance uncertainties and hence FIR luminosity uncertainties, we measure a correlation coefficient of 0.53 and 0.90 respectively.

The non-thermal radio emission is a more direct indicator of the supernova rate and hence high-mass star formation (e.g. Condon & Yin 1990). Therefore we also investigate the correlation between the 1.4 GHz radio emission of the galaxies in our sample with the detected number of X-ray SNRs (Fig. 14). We use integrated radio fluxes from Condon (1987) and we find a correlation coefficient of 0.45. For the same reasons described in the previous paragraph, if we remove NGC 2403 or NGC 4449 the correlation coefficient is 0.22 and 0.85 respectively. The weaker correlation between the number of SNRs and the radio 1.4 GHz luminosity could be due to a significant contribution of thermal radio emission to the 1.4 GHz luminosity.

5.4. Luminosity distribution of SNRs

In order to examine our results in the context of SNR populations detected in other galaxies, we compare the luminosity distributions of X-ray SNRs in different types of galaxies with the number of X-ray detected SNRs in the studied sample. Therefore we test if the numbers of SNRs in the irregular galaxies in our sample are consistent with those expected, by simply rescaling the SNR X-ray luminosity Functions (XLFs) of the MCs (Ghavamian et al. 2005).

We can estimate the expected number of SNRs in the galaxies of our sample based on a Magellanic Cloud - like SNR luminosity function and linear scaling of their number with star-formation rate. We find that the number of the observed SNRs in most galaxies of our sample is consistent with those expected by rescaling the MC XLF (Table 25), which has a cumulative slope of -0.5 (Ghavamian et al. 2005). However, we see a large discrepancy between the observed and expected number of SNRs in NGC 4449 and NGC 2403. In the case of NGC 4449, this discrepancy could be due to the significant distance uncertainty to this galaxy which ranges between 2.9

(Karachentsev & Drozdovsky 1998) and 5.0 Mpc (Aaronson & Mould 1983). The lowest distance value of 2.9 Mpc has been used in previous X-ray SNR surveys (e.g. Summers et al. 2003) and the corresponding expected number of SNRs (6.75) is in fair agreement with the observed number (3). A more reliable measurement of its distance based on the TRGB (Tip of the Red Giant Branch) method (4.2 Mpc; Annibali et al. 2008) results in 13.8 SNRs (see Table 25). Given the large uncertainties in its distance we exclude NGC 4449 from this comparison.

In the case of NGC 2403, the discrepancy of the observed population of X-ray selected SNRs with these expected based on the MC XLF and a linear scaling with SFR, may indicate a difference between their populations. Such a difference might be expected given that NGC 2403 is a grand design spiral galaxy, while the MCs are irregular galaxies. Therefore we use, instead of the MCs, the XLF of SNRs of M33 as our benchmark (Haberl & Pietsch 2001). Since this XLF is not based on X-ray selected SNRs but instead optically/radio selected SNRs, for consistency we compare them with the SNR census of Pannuti et al. which is based on similar selection criteria. This also allows us to extend the comparison to a larger number of spiral galaxies. We follow the same approach as for the irregular galaxies with the only exception that we rescaled the number of M33 SNRs to the limiting luminosity of Pannuti et al. (2007) (10^{37} erg s $^{-1}$). We find a good agreement between the observed numbers of optically/radio selected SNRs in these spiral galaxies and the ones expected based on an M33-like XLF (Table 26).

Overall, our comparisons of the luminosity distributions of X-ray selected SNRs in different types of galaxies with the number of X-ray detected SNRs in the studied sample is suggestive of different luminosity distributions between the SNRs in spiral and irregular galaxies. This will be further examined by the comparison of the XLFs between SNRs in the spiral and irregular galaxies of our sample (Leonidaki et al. in preparation).

6. Conclusions–Summary

1. In this paper we have presented a systematic study of X-ray emitting SNRs in a sample of six nearby galaxies. The SNRs are selected on

the basis of their soft X-ray spectra ($kT < 2$ keV) or colors. We find a total of 37 X-ray SNRs, 30 of which are new identifications. Many of these SNRs are also detected in other wavebands which indicates that the X-ray colors are a good diagnostic for the primary identification of thermal SNRs. From the analysis of the sample we find: 22% of the optically identified SNRs and 37% of the radio candidate SNRs have X-ray counterparts. There is little overlap (5%) between optical and radio classifications, which could primarily be due to the poor sensitivity of the existing radio surveys.

2. Four sources identified as SNRs in optical or radio observations exhibit X-ray properties more consistent with XRBs. The latter and SNRs can be naturally associated since they are both related to short-lived high mass stellar objects, therefore we propose that these sources are X-ray binaries coincident with a supernova remnant.

3. We do not find any trend between the X-ray luminosity of SNRs and their HI column density or temperature.

4. We find that X-ray SNRs in irregular galaxies appear to be more luminous than those in spiral galaxies. We attribute this effect either to the lower metallicity of irregular galaxies (which result in more massive progenitors) or their clumpy ISM.

5. We find evidence for a linear relation between the number of luminous X-ray SNRs ($L_x > 5 \times 10^{36}$ erg s $^{-1}$) and star-formation rate in our sample of galaxies.

6. There is a suggestion for different X-ray luminosity functions between the SNR populations of irregular and spiral galaxies, based on comparison of the observed numbers of SNRs and those expected by rescaling the luminosity functions of SNRs in the MCs.

The authors would like to thank John Raymond for fruitful discussions. This work was partly supported by NASA grant GO6-7086X and NASA LTSA grant G5-13056. IL and PB would like to thank the Harvard–Smithsonian Center for Astrophysics for its hospitality during their visits there. IL acknowledges funding by the European Union and the Greek Ministry of Development in the framework of the programme ‘Promotion of Excellence in Research Institutes (2nd Part).

REFERENCES

- Aaronson, M. & Mould, J. 1983, *ApJ*, 265, 1
- Annibali, F., Aloisi, A., Mack, J., Tosi, M., van der Marel, R.P., Angeretti, L., Leitherer, C., Sirianni, M. 2008, *AJ*, 135, 1900
- Asaoka, I. & Koyama, K. 1990, *PASJ*, 42, 625
- Balick, B. & Heckman, T. 1978, *ApJ*, 226, L7
- Blair, W.P., Kirshner, R.P. & Chevalier, R.A. 1982, *ApJ*, 254, 50
- Blair, W.P., Kirshner, R.P. & Winkler, P.F. 1983, *ApJ*, 272, 84
- Blair, W.P., Raymond, J.C., Fesen, R.A. & Gull, T.R. 1984, *ApJ*, 279, 708
- Blair, W.P. & Long, K.S. 1997, *ApJS*, 108, 262
- Blair, W.P. & Long, K.S. 2004, *ApJS*, 155, 101
- Bykov, A.M. 2005, in *IAU Symp.230, Populations of High Energy Sources in Galaxies*, edited by Meurs, E.J.A., Fabbiano, G., p111
- Cash, W. 1979, *ApJ*, 228, 939
- Charles, P.A. & Seward, F.D., *Exploring the X-ray Universe*, Cambridge University Press, 1995
- Chevalier, R.A. & Fransson, C. 2001, *ApJ*, 558, 27
- Chomiuk, L. & Wilcots, E.M. 2009, *AJ*, 137, 3869
- Chu, Y.H. 1995 in 11th IAP Astrophysics Meeting, The interplay between massive star formation, the ISM and galaxy evolution, edited by Kunth, D., Guiderdoni, B., Heydari-Malayeri M., Thuan, T.X., p.201
- Condon, J.J., 1987, *ApJS*, 65, 485
- Condon, J.J. & Yin, Q.F., 1990, *ApJ*, 357, 97
- Cutri, R.M. et al. 2003, The IRSA 2MASS All Sky Catalog of point sources, NASA/IPAC Infrared Science Archive. <http://irsa.ipac.caltech.edu/applications/Gator/>
- de Vaucouleurs G., de Vaucouleurs A., Corwin H.G., Buta R.J., Paturel G., Fouque P., 1995, Third Reference Catalog of Bright Galaxies (RC3) (de Vaucouleurs+ 1991)
- Dickel, J.R., 1999, in *IAU Symp.190, New views of the Magellanic Clouds*, edited by Chu, Y.H., Suntzeff, N.B., Hesser, J.E. & Bohlender, D.A., p139
- Di Stefano, R., & Kong, A.K.H. 2004, *ApJ*, 609, 710
- D’Odorico, S., Dopita, M.A. & Benvenuti, P. 1980, *A&AS*, 40, 67
- Eck, C.R., Cowan, J.J., & Branch, D. 2002, *ApJ*, 573, 306
- Freedman, W.L., & Madore, B.F. 1988, *ApJ*, 332, L63
- Freedman, W.L., et al. 1994, *ApJ*, 427, 628
- Garmire, G.P., Bautz, M.W., Ford, P.G., Nousek, J.A. & George R. Ricker, Jr. 2003, *Proc, SPIE*, 4851, 28
- Garnett, D.R. 2002, *ApJ*, 581, 1019
- Ghavamian, P., Blair, W.P., Long, K.S., Sasaki, M., Gaetz, T.J. & Plucinsky, P., 2005, *AJ*, 130, 539
- Green, D.A. 2009, *Bulletin of the Astronomical Society of India*, 37, 45. (See: arXiv:0905.3699)
- Greiner, J., *Supersoft X-ray Sources*, Springer, 1996
- Haberl & Pietsch 2001, *A&A*, 373, 438
- Helou, G., Khan, I.R., Malek, L., & Boehmer, L. 1988, *ApJS*, 68, 151
- Ho, L.C., Filippenko, A.V. & Sargent, W.L.W. 1997, *ApJS*, 112, 315
- Immler, S., Wang, Q.D., Leonard, D.C. & Schlegel, E.M. 2003, *ApJ*, 595, 727
- Kalberla, P.M.W., Burton, W.B., Hartmann, Dap, Arnal, E.M., Bajaja, E., Morras, R., Poppel, W.G.L. 2005, *A&A*, 440, 775
- Karachentsev, I.D., Drozdovsky, I.O. 1998, *A&AS*, 131, 1
- Kim, M., Wilkes, B.J., Kim, D., Green, P.J., Barkhouse, W.A., Lee, M.G., Silverman, J.D., Tanabbaum, H.D. 2007, *ApJ*, 659, 29

- Kirshner, R.P. & Blair, W.P. 1980, *ApJ*, 236, 135
- Kong, A.K.H., Garcia, M.R., Primini, F.A. & Murray, S.S. 2002, *ApJ*, 580, L125
- Kong, A.K.H., Siouwerman, L.O. & Williams, B.F. 2004, *AJ*, 128, 2783
- Lacey, C.K., Goss, W.M. & Mizouni, L.K. 2007, *AJ*, 133, 2156
- Lamers, H.J.G.L.M., & Cassinelli, J.P., *Introduction to Stellar Winds*, Cambridge University Press, 1999
- Matonick, D.M. & Fesen, R.A. 1997, *ApJS*, 112, 49
- Matonick, D.M., Fesen, R.A., Blair, W.R. & Long, K.S. 1997, *ApJS*, 113, 333
- Ott, J., Martin, C.L. & Walter, F. 2003, *ApJ*, 594, 776
- Pagel, B.E.J., & Endmunds, M.G. 1981, *ARA&A*, 19, 77
- Pannuti, T.G., Duric, N., Lacey, C.K., Goss, W.M., Hoopes, C.G., Walterbos, R.A.M. & Magnor, M.A. 2000, *ApJ*, 544, 780
- Pannuti, T.G., Duric, N., Lacey, C.K., Ferguson, A.M.N., Magnor, M.A. & Mendelowitz, C. 2002, *ApJ*, 565, 966
- Pannuti, T.G., Schlegel, E.M., & Lacey, C.K. 2007, *AJ*, 133, 1361
- Park, T., Kashyap, V.L., Siemiginowska, A., van Dyk, D.A., Zezas, A., Heinke, C. & Wargelin, B.J. 2006, *ApJ*, 652, 610
- Patnaude, D.J., & Fesen, R.A. 2003, *ApJ*, 587, 221
- Payne, J.L., Filipović, M.D., Pannuti, T., Jones, P.A., Duric, N., White, J.L. & Carpano, S. 2004, *A&A*, 425, 443
- Protassov, R. & van Dyk, D.A. 2002, *ApJ*, 571, 545
- Rice, W., Lonsdale, C.J., Soifer, B.T., Neugebauer, G., Kopan, E.L., Lloyd, L.A., de Jong, T. & Habing, H.J. 1988, *ApJS*, 68, 91
- Rosa-González, D. 2005, *MNRAS*, 364, 1304
- Safi-Harb, S. & Petre, R. 1999 *ApJ*, 512, 784
- Safi-Harb, S., Harrus, I.M., Petre, R., Pavlov, G.G., Koptsevich, A.B., Samwal, D. 2001, *ApJ*, 561, 308
- Saha, A., Labhardt, L., Schwengeler, H., Macchetto, F.D., Panagia, N., Sandage, A. & Tammann, G.A. 1994, *ApJ*, 425, 14
- Schlegel, E.M. 1994, *AJ*, 434, 523
- Schlegel, E.M., Blair, W.P. & Fesen, R.A. 2000, *AJ*, 120, 791
- Schlegel, E.M. & Pannuti, T.G., 2003, *AJ*, 125, 3025
- Smith, R.K., Brickhouse, N.S., Liedahl, D.A., Raymond, J.C. 2001, *ApJ*, 556, 91
- Sramek, R. 1992, *Relationships between Active Galactic Nuclei and Starburst Galaxies*, ed. A.V. Filipenko, ASP Conference Series (ASP: San Francisco), 31, p.273
- Stupar, M. & Parker, Q.A., 2009, *MNRAS*, 394, 1791
- Summers, L.K., Stevens, I.R., Strickland, D.K. & Heckman, T.M. 2003, *MNRAS*, 342, 690
- Swartz, D.A., Chosh, K.K., McCollough, M.L., Pannuti, T.G., Tennant, A.F. & Wu, K. 2003, *ApJS*, 144, 213
- Tully, R. 1988, *Nearby galaxies Catalog* (Cambridge: Cambridge University Press)
- Turner, J.L. & Ho, P.T.P. 1994, *ApJ*, 421, 122
- van Dyk, D.A., Connors, A., Kashyap, V.L. & Siemiginowska, A. 2001, *ApJ*, 548, 224
- van Speybroeck, L.P., Jerius, D., Edgar, R.J., Gaetz, T.J. & Zhao, P. 1997, *SPIE*, 3113, 89
- Vogler, A. & Pietsch, W. 1997, *A&A*, 319, 459
- Vukotić, B., Bojičić, I., Pannuti, T.G. & Urošević, D. 2005, *SerAJ*, 170, 101
- Walter, F., Weiss, A., Martin, C. & Scoville, N. 2002, *AJ*, 123, 225
- Winter, L.M., Mushotzky, R.F. & Reynolds, C.S. 2006, *ApJ*, 649, 730

Yokogawa, J., Imanishi, K., Tsujimoto, M., Nishiuchi, M., Koyama, K., Nagase, F., & Corbet, R.H.D., 2000, *ApJS*, 128, 491

Zezas, A., Fabbiano, G., Baldi, A., Schweizer, F., King, A.R., Ponman, T.J. & Rots, A.H. 2006, *ApJS*, 166, 211

TABLE 1
 PROPERTIES OF OUR SAMPLE OF GALAXIES

Galaxy	RA (J2000)	DEC (J2000)	Distance (Mpc)	Major and Minor axis (arcmin)	Inclination ^a (degrees)	Galactic N _H ^b ($\times 10^{20}$ cm ⁻²)	Galactic latitude (degrees)	Position Angle ^c (degrees)	Type	Physical scale ^d (pc)
NGC 2403	07:36:51.4	65:36:09	3.2 ^e	21.9 \times 12.3	62	4.36	29	127	SAB(s)cd	7.7
NGC 5204	13:29:36.5	58:25:07	4.8 ^e	5.0 \times 3.0	53	1.75	58	5	SA(s)m	11.5
NGC 4395	12:25:48.9	33:32:48	2.6 ^f	13.2 \times 11.0	38	1.85	82	147	SA(s)m	6.2
NGC 4449	12:28:11.9	44:05:40	4.2 ^g	6.2 \times 4.4	56	1.61	72	45	IBm	10.1
NGC 3077	10:03:19.1	68:44:02	3.6 ^h	5.4 \times 4.5	...	5.05	42	45	I0 pec	8.6
NGC 4214	12:15:39.2	36:19:37	4.7 ⁱ	8.5 \times 6.6	37	1.99	78	...	IAB(s)m	11.3

NOTE.—Units of right ascension are hours, minutes and seconds and units of declination are degrees, arcminutes and arcseconds. We note that the SA(s)m galaxies are Magellanic-type which are classified as irregulars with some spiral structure. Coordinates, diameters, Galactic latitudes and types of galaxies are from *NED*.

^aTully (1988) apart from NGC 4449 (Summers et al. 2003)

^b(Leiden/Argentine/Bonn) LAB Survey of Galactic HI

^cThird Reference Catalog of Bright Galaxies

^dPhysical scales corresponding to 0.5'' at the distance of each galaxy

^eFreedman & Madore (1988)

^fSaha et al. (1994)

^gAnnibali et al. (2008)

^hFreedman et al. (1994)

ⁱTully (1988)

TABLE 2
COMPARISON OF SNRS DETECTED IN THIS STUDY WITH PREVIOUS STUDIES

Galaxy	Number of Optically Identified SNRs	Number of candidate radio SNRs	Number of X-ray Identified SNRs	Number of X-ray selected SNRs in this study *
NGC 2403	35 ^a	3 ^b	1 ^c	15 (0)
NGC 5204	3 ^d	0	0	0
NGC 4395	0	1 ^e	0	2 (1)
NGC 4449	1 ^f	8 ^g	2 ^h	4 (0)
NGC 3077	0	1 ⁱ	3 ^j	5 (0)
NGC 4214	0	7 ^e	0	11 (4)

*The numbers in parenthesis are the candidate SNRs in relation to the total (see Section 4 for the classification of X-ray SNRs).

References: (a) D’Odorico et al. (1980); Matonick et al. (1997); (b) Turner & Ho (1994); Eck et al. (2002); (c) Schlegel & Pannuti (2003); Pannuti et al. (2007); (d) Matonick & Fesen (1997); (e) Vukotić et al. (2005); Chomiuk & Wilcots (2009); (f) Balick & Heckman (1978); Kirshner & Blair (1980); Blair et al. (1983); (g) Lacey et al. (2007); Chomiuk & Wilcots (2009); (h) Vogler & Pietsch (1997); Patnaude & Fesen (2003); Summers et al. (2003); (i) Rosa-González (2005); (j) Ott et al. (2003)

TABLE 3
Chandra OBSERVATION LOG

Galaxy	Observation Number	Obs ID	Net Exposure (ksec)	Date	Roll
Single Exposures					
NGC 3077	1	2076	54.14	2001 Mar 07	199.5
NGC 4449	1	2031	26.94	2001 Feb 04	108.8
NGC 4395	1	882	17.19	2000 Jun 20	253.8
Multiple Exposures					
NGC 4214	1	2030	26.76	2001 Oct 16	23.9
	2	4743	27.56	2004 Apr 03	193.1
	3	5197	28.96	2004 Jul 30	275.8
NGC 2403	1	2014	36.00	2001 Apr 17	266.8
	2	4628	47.12	2004 Aug 23	44.5
	3	4629	45.14	2004 Oct 03	75.2
	4	4630	50.58	2004 Dec 22	149.3
NGC 5204	1	2028	10.15	2001 Jan 09	77.3
	2	2029	9.55	2001 May 02	197.7
	3	3933	48.94	2003 Aug 06	281.2
	4	3934	5.01	2003 Aug 09	284.4
	5	3935	4.76	2003 Aug 11	287.0
	6	3936	4.83	2003 Aug 14	290.0
	7	3937	4.91	2003 Aug 17	292.8
	8	3938	5.45	2003 Aug 19	295.7
	9	3939	5.44	2003 Aug 27	304.2
	10	3940	5.13	2003 Sep 05	314.3
	11	3941	5.16	2003 Sep 14	324.2
	12	3942	5.51	2003 Sep 23	334.0
	13	3943	5.18	2003 Oct 03	345.5

TABLE 4
NUMBER OF BACKGROUND SOURCES FOR THE GALAXIES IN OUR SAMPLE

Galaxy	Expected background sources
NGC 2403	60
NGC 5204	3
NGC 4395	0
NGC 4449	7.6
NGC 3077	6
NGC 4214	15.6

NOTE.—Based on the 0.5 - 2.0 keV $\log N$ - $\log S$ of Kim et al. (2007), we estimated the number of background sources within the area of each galaxy covered by the *Chandra* observations. The *Chandra* data cover the entire D_{25} area of NGC 4214 and NGC 4449, 30% of NGC 4395 and 80 - 90% of NGC 2403, NGC 3077 and NGC 5204.

TABLE 5
PHOTOMETRIC PROPERTIES OF POTENTIAL SNRS IN NGC 3077

Src.ID	RA (h:m:s)	DEC (d:m:s)	Soft Band		Medium Band		Hard Band		Total Band		Area	Effective Area
			Obs Counts	Bkg Counts	Obs Counts	Bkg Counts	Obs Counts	Bkg Counts	Obs Counts	Bkg Counts		
LZB_2	10:03:17.73	+68:44:16.57	35	202	0	77	0	30	35	309	159.1	1.01
LZB_6	10:03:18.08	+68:44:04.04	17	295	6	129	0	38	23	462	127.7	1.02
LZB_8	10:03:21.19	+68:46:33.27	3	72	3	55	0	89	6	216	1035.	0.99
LZB_12	10:03:21.82	+68:45:03.29	5	88	7	53	0	76	12	217	424.6	0.99
LZB_13	10:03:12.14	+68:43:19.07	1	65	7	74	2	70	10	209	652.5	0.99
LZB_14	10:03:08.25	+68:44:08.57	8	47	15	44	5	53	28	144	395.0	0.99
LZB_15	10:03:20.60	+68:41:40.29	75	49	109	60	23	73	207	182	213.0	0.99
LZB_18	10:03:18.62	+68:43:56.87	29	295	86	129	11	38	126	462	182.2	1.02
LZB_19	10:02:56.51	+68:44:30.59	33	61	69	48	35	83	137	192	149.8	0.97

NOTE.—Column 1: Source ID; Columns 2-3: Source coordinates in J2000; Cols 4-11: Photometric counts of each source and its background in the soft, medium, hard and total bands respectively (see Section 3.3); Column 12: (Background / source) area ratio; Column 13: Effective area ratio with respect to a reference point (see §3.3) in the soft energy band.

TABLE 6
PHOTOMETRIC PROPERTIES OF POTENTIAL SNRS IN NGC 4395

Src.ID	RA (h:m:s)	DEC (d:m:s)	Soft Band		Medium Band		Hard Band		Total Band		Area	Effective Area
			Obs Counts	Bkg Counts	Obs Counts	Bkg Counts	Obs Counts	Bkg Counts	Obs Counts	Bkg Counts		
LZB_1	12:25:54.52	+33:30:44.29	16	62	2	27	0	32	18	121	597.5	1.00
LZB_2	12:25:45.15	+33:31:02.51	47	62	0	22	0	37	47	121	409.5	0.99
LZB_5	12:25:47.01	+33:36:06.22	21	59	14	29	2	65	37	153	232.5	0.99
LZB_6	12:25:40.90	+33:31:09.50	3	40	4	20	1	26	8	86	531.9	0.97
LZB_7	12:25:55.03	+33:30:15.02	1	42	3	23	0	21	4	86	1354.	1.25
LZB_10	12:25:53.22	+33:38:30.37	1	41	1	24	0	26	2	91	2492.	0.99
LZB_12	12:25:59.77	+33:33:20.57	35	131	39	123	8	39	82	293	292.6	1.76
LZB_14	12:25:39.42	+33:32:03.55	95	43	78	40	5	34	178	117	326.8	1.00
LZB_15	12:25:48.93	+33:32:00.81	85	58	114	41	48	60	247	159	471.4	0.99

NOTE.—For the description of the columns see Table 5.

TABLE 7
PHOTOMETRIC PROPERTIES OF POTENTIAL SNRS IN NGC 4449

Src_ID	RA (h:m:s)	DEC (d:m:s)	Soft Band		Medium Band		Hard Band		Total Band		Area	Effective Area
			Obs Counts	Bkg Counts	Obs Counts	Bkg Counts	Obs Counts	Bkg Counts	Obs Counts	Bkg Counts		
LZB_2	12:28:07.35	+44:04:53.40	94	91	50	26	9	18	153	135	74.4	0.98
LZB_4	12:28:11.93	+44:06:40.86	74	281	94	93	17	23	185	397	148.9	0.99
LZB_5	12:28:11.18	+44:06:37.67	66	281	40	93	6	23	112	397	94.3	0.99
LZB_8	12:28:13.23	+44:06:55.27	100	260	135	100	17	20	252	380	109.9	0.97
LZB_9	12:28:11.99	+44:05:57.74	37	165	20	47	2	14	59	226	71.9	1.00
LZB_11	12:28:10.94	+44:04:59.06	3	181	16	46	5	17	24	244	275.1	1.45
LZB_12	12:28:10.97	+44:06:47.80	378	281	568	93	86	23	1032	397	82.4	0.99
LZB_13	12:28:10.93	+44:03:37.58	403	74	2	37	0	50	405	161	107.6	0.99
LZB_14	12:28:10.38	+44:05:58.02	39	149	1	30	0	12	40	191	80.28	1.00
LZB_15	12:28:09.69	+44:05:52.80	44	137	110	30	46	20	200	187	76.67	0.99
LZB_16	12:28:09.28	+44:05:07.96	565	229	555	61	57	18	1177	308	216.0	0.98
LZB_18	12:28:06.81	+44:05:28.03	3	78	9	17	2	12	14	107	283.8	0.99
LZB_20	12:28:16.35	+44:07:38.47	3	61	1	28	3	41	7	130	904.9	0.97
LZB_21	12:28:01.32	+44:05:29.85	4	74	10	21	0	24	14	119	379.5	0.99
LZB_22	12:28:23.98	+44:04:54.78	4	69	0	45	1	67	5	181	959.4	0.99
LZB_24	12:28:11.23	+44:05:36.69	6	182	1	52	0	18	7	252	186.6	0.99
LZB_25	12:28:18.99	+44:05:44.32	40	173	0	51	0	42	40	266	375.4	0.93
LZB_26	12:28:15.58	+44:05:36.34	12	435	3	63	1	28	16	526	506.3	0.95

NOTE.—For the description of the columns see Table 5.

TABLE 8
PHOTOMETRIC PROPERTIES OF POTENTIAL SNRS IN NGC 4214

Src_ID	RA (h:m:s)	DEC (d:m:s)	Soft Band		Medium Band		Hard Band		Total Band		Area	Effective Area
			Obs Counts	Bkg Counts	Obs Counts	Bkg Counts	Obs Counts	Bkg Counts	Obs Counts	Bkg Counts		
LZB_5	12:15:40.82	+36:19:26.29	10	2490	2	1534	4	1861	16	5885	4939.6	1.00
LZB_7	12:15:33.41	+36:18:58.88	50	925	5	809	3	1229	58	2963	1158.3	0.98
LZB_10	12:15:49.71	+36:18:46.69	3	924	5	788	1	1177	9	2889	3948.4	0.99
LZB_11	12:15:37.93	+36:22:21.00	2	867	5	884	0	1091	7	2842	4956.7	0.98
LZB_16	12:15:40.16	+36:19:25.21	4	2490	3	1534	0	1861	7	5885	6656.5	1.05
LZB_20	12:15:38.13	+36:20:50.08	6	1047	19	955	5	1335	30	3337	3237.0	1.04
LZB_23	12:15:48.80	+36:17:01.83	2	834	8	883	1	1437	11	3154	4187.0	0.96
LZB_24	12:15:41.37	+36:21:13.67	135	1047	235	955	110	1335	480	3337	435.43	0.98
LZB_25	12:15:38.24	+36:19:20.44	573	2490	1042	1534	362	1861	1977	5885	797.84	0.97
LZB_26	12:15:38.11	+36:19:44.03	99	2490	258	1534	69	1861	426	5885	865.80	1.03
LZB_27	12:15:43.56	+36:20:09.35	12	2490	9	1534	0	1861	21	5885	4052.9	0.98
LZB_28	12:15:41.86	+36:19:14.47	13	2490	13	1534	1	1861	27	5885	3263.6	0.97
LZB_29	12:15:40.85	+36:19:38.84	15	2490	52	1534	22	1861	89	5885	2285.5	1.00
LZB_30	12:15:39.97	+36:18:40.12	36	924	4	788	0	1177	40	2889	1470.7	0.98
LZB_31	12:15:39.37	+36:20:54.09	26	1047	6	955	2	1335	34	3337	1686.6	0.98
LZB_33	12:15:44.74	+36:18:46.00	10	924	57	788	29	1177	96	2889	977.95	0.98
LZB_34	12:15:40.01	+36:19:35.78	54	2490	20	1534	5	1861	79	5885	1051.5	1.06
LZB_35	12:15:37.23	+36:22:18.65	35	867	21	884	2	1091	58	2842	744.23	0.99
LZB_37	12:15:34.36	+36:22:19.02	35	867	115	884	47	1091	197	2842	453.00	0.98
LZB_38	12:15:45.65	+36:19:42.21	10	2490	2	1534	0	1861	12	5885	3441.3	0.99
LZB_41	12:15:36.05	+36:18:47.25	5	925	0	809	11	1229	16	2963	1492.3	1.00
LZB_43	12:15:47.74	+36:21:55.11	2	1217	13	1227	5	1523	20	3967	1729.9	0.94

NOTE.—For the description of the columns see Table 5.

TABLE 9
PHOTOMETRIC PROPERTIES OF POTENTIAL SNRS IN NGC 2403

Src_ID	RA (h:m:s)	DEC (d:m:s)	Soft Band		Medium Band		Hard Band		Total Band		Area	Effective Area
			Obs Counts	Bkg Counts	Obs Counts	Bkg Counts	Obs Counts	Bkg Counts	Obs Counts	Bkg Counts		
LZB_2	07:37:10.70	+65:33:11.73	28	1816	49	1598	10	2340	87	5754	781.4	0.95
LZB_5	07:36:52.44	+65:36:41.69	34	4482	7	2854	2	3418	43	10754	2574.	0.97
LZB_14	07:37:16.43	+65:33:29.24	28	1818	12	1609	1	2346	41	5773	1090.	0.98
LZB_21	07:38:00.72	+65:32:09.30	81	519	148	491	42	785	271	1795	241.7	1.18
LZB_30	07:36:46.13	+65:36:41.80	32	4482	17	2854	1	3418	50	10754	1035.	0.95
LZB_39	07:36:35.95	+65:36:09.35	27	4482	56	2854	20	3418	103	10754	1368.	1.18
LZB_41	07:37:13.50	+65:35:58.72	49	3543	12	2389	4	3112	65	9044	2123.	0.98
LZB_42	07:36:57.54	+65:36:04.45	37	4482	24	2854	2	3418	63	10754	2149.	0.91
LZB_54	07:37:40.85	+65:35:22.39	29	1425	158	1301	75	1966	262	4692	1237.	1.03
LZB_58	07:36:46.49	+65:36:14.33	15	4482	71	2854	47	3418	133	10754	1058.	0.96
LZB_63	07:37:38.78	+65:36:30.67	134	1425	0	1301	1	1966	135	4692	1764.	1.01
LZB_64	07:36:34.47	+65:38:55.66	268	1444	294	871	75	1397	637	3712	255.3	0.97
LZB_65	07:37:37.39	+65:32:01.36	60	1545	91	1373	31	1943	182	4861	509.8	1.12
LZB_68	07:37:15.12	+65:32:02.71	13	814	1	584	1	984	15	2382	1608.	0.91
LZB_69	07:37:33.81	+65:33:07.69	348	1680	497	1613	166	2194	1011	5487	438.6	1.03
LZB_71	07:37:22.24	+65:33:18.48	363	1680	6	1613	6	2194	375	5487	742.6	0.82
LZB_72	07:37:10.01	+65:33:06.01	140	1816	1	1598	3	2340	144	5754	758.7	0.95
LZB_75	07:37:18.23	+65:37:27.27	15	3207	4	2988	3	4343	22	10538	4116.	0.93
LZB_76	07:37:17.92	+65:36:24.17	20	3543	9	2389	0	3112	29	9044	3086.	0.99
LZB_78	07:37:07.96	+65:39:20.63	69	3000	24	2918	3	4577	96	10495	2190.	0.75
LZB_80	07:37:03.39	+65:34:38.57	21	2542	6	1705	2	2104	29	6351	1515.	1.04
LZB_81	07:37:02.99	+65:37:11.31	37	3543	12	2389	1	3112	50	9044	2617.	1.00
LZB_86	07:37:02.71	+65:36:02.58	18	3543	4	2389	3	3112	25	9044	2938.	0.98
LZB_93	07:37:01.18	+65:34:17.91	186	2542	136	1705	45	2104	367	6351	574.8	1.00
LZB_98	07:37:15.24	+65:34:29.94	111	2491	369	2148	156	3044	636	7683	1450.	0.94
LZB_99	07:37:12.02	+65:33:46.28	132	1818	928	1609	412	2346	1472	5773	479.5	0.99
LZB_100	07:37:09.48	+65:35:45.09	95	3543	425	2389	371	3112	891	9044	888.5	0.98
LZB_101	07:37:07.74	+65:34:56.37	211	2542	205	1705	95	2104	511	6351	943.0	0.98
LZB_103	07:37:02.63	+65:39:36.34	098	3000	3205	2918	1733	4577	6036	10495	521.2	0.72
LZB_104	07:36:55.97	+65:35:41.68	388	4482	6568	2854	2416	3418	1372	10754	257.9	0.91
LZB_105	07:36:50.43	+65:36:04.59	216	4482	447	2854	103	3418	766	10754	773.0	1.09
LZB_107	07:36:42.39	+65:36:52.58	586	4482	266	2854	4	3418	856	10754	715.1	0.97
LZB_109	07:36:25.94	+65:35:40.28	110	1516	11671	1384	3825	1712	8606	4612	103.9	0.97
LZB_112	07:37:27.66	+65:31:02.52	118	1149	280	1032	112	1531	510	3712	234.8	0.81
LZB_115	07:36:32.84	+65:39:01.95	43	1444	83	871	44	1397	170	3712	526.1	0.93
LZB_120	07:36:47.95	+65:36:22.35	96	4482	130	2854	53	3418	279	10754	460.0	0.95

NOTE.—For the description of the columns see Table 5.

TABLE 10
PHOTOMETRIC PROPERTIES OF POTENTIAL SNRS IN NGC 5204

Src.ID	RA (h:m:s)	DEC (d:m:s)	Soft Band		Medium Band		Hard Band		Total Band		Area	Effective Area
			Obs Counts	Bkg Counts	Obs Counts	Bkg Counts	Obs Counts	Bkg Counts	Obs Counts	Bkg Counts		
LZB_8	13:29:39.26	+58:25:31.20	94	834	47	595	9	586	150	2015	235.7	0.98
LZB_10	13:29:38.63	+58:25:05.51	14427	1182	13451	834	2191	846	30069	2862	71.6	0.99
LZB_11	13:29:27.47	+58:25:34.26	86	125	124	144	56	275	266	544	91.9	0.99

NOTE.—For the description of the columns see Table 5.

TABLE 11
X-RAY COLORS FOR POTENTIAL SNRS IN NGC 3077

Source_ID	Col(S/M)	Col(M/H)	Col(S/H)	Spectra	Classification	Counterpart
LZB_2	$1.84^{+0.95}_{-0.57}$	$0.00^{+1.18}_{-1.18}$	$1.84^{+0.95}_{-0.57}$	Yes	SSS	SSS (Ott-S4) ^a
LZB_6	$0.44^{+0.26}_{-0.23}$	$1.03^{+0.98}_{-0.61}$	$1.48^{+0.95}_{-0.58}$	Yes	probable SNR	SNR (Ott-S6) ^a
LZB_8	$0.00^{+0.35}_{-0.35}$	$0.84^{+0.98}_{-0.64}$	$0.84^{+0.98}_{-0.64}$	Yes	XRB	...
LZB_12	$-0.14^{+0.25}_{-0.26}$	$1.16^{+0.96}_{-0.58}$	$1.03^{+0.96}_{-0.61}$	Yes	probable SNR	...
LZB_13	$-0.72^{+0.41}_{-0.54}$	$0.49^{+0.38}_{-0.33}$	$-0.23^{+0.54}_{-0.60}$	Yes	probable SNR	...
LZB_14	$-0.26^{+0.18}_{-0.19}$	$0.46^{+0.23}_{-0.21}$	$0.19^{+0.25}_{-0.24}$	Yes	XRB	...
LZB_15	$-0.16^{+0.09}_{-0.22}$	$0.68^{+0.10}_{-0.10}$	$0.51^{+0.10}_{-0.10}$	Yes	probable SNR	...
LZB_18	$-0.49^{+0.09}_{-0.10}$	$0.88^{+0.15}_{-0.13}$	$0.39^{+0.16}_{-0.15}$	Yes	probable SNR	SNR (Ott-S1) ^{a, b}
LZB_19	$-0.32^{+0.09}_{-0.09}$	$0.30^{+0.09}_{-0.09}$	$-0.024^{+0.11}_{-0.10}$	Yes	XRB	...

NOTE.—Column 1: Source ID; Columns 2-4: X-ray colors and their errors (derived from the BEHR method) in the Soft/Medium, Medium/Hard and Soft/Hard bands respectively; Column 5: Whether spectrum of the source is derived; Column 6: The classification of the source according to its spectrum (see §3.4.2 and §4) and Column 7: Multiwavelength associations

^aSources identified by Ott et al. (2003).

^bRadio candidate SNR by Rosa-González (2005)

TABLE 12
X-RAY COLORS FOR POTENTIAL SNRS IN NGC 4395

Source_ID	Col(S/M)	Col(M/H)	Col(S/H)	Spectra	Classification	Counterpart
LZB_1	$0.82^{+0.34}_{-0.28}$	$0.69^{+0.99}_{-0.67}$	$1.52^{+0.95}_{-0.57}$	Yes	XRB	...
LZB_2	$1.97^{+0.95}_{-0.55}$	$0.00^{+1.18}_{-1.18}$	$1.97^{+0.95}_{-0.55}$	Yes	XRB	...
LZB_5	$0.17^{+0.15}_{-0.15}$	$0.80^{+0.42}_{-0.32}$	$0.97^{+0.41}_{-0.32}$	Yes	XRB	...
LZB_6	$-0.11^{+0.32}_{-0.34}$	$0.49^{+0.52}_{-0.43}$	$0.37^{+0.54}_{-0.44}$	Yes	XRB	...
LZB_7	$-0.37^{+0.43}_{-0.52}$	$0.84^{+0.98}_{-0.63}$	$0.46^{+1.04}_{-0.77}$	Yes	XRB	...
LZB_10	$0.00^{+0.57}_{-0.58}$	$0.47^{+1.03}_{-0.75}$	$0.47^{+1.03}_{-0.77}$	No	candidate SNR ^a	...
LZB_12	$-0.05^{+0.10}_{-0.10}$	$0.67^{+0.17}_{-0.16}$	$0.62^{+0.18}_{-0.16}$	Yes	XRB	...
LZB_14	$0.09^{+0.06}_{-0.07}$	$1.16^{+0.21}_{-0.18}$	$1.25^{+0.21}_{-0.18}$	Yes	SNR	...
LZB_15	$-0.13^{+0.06}_{-0.06}$	$0.37^{+0.08}_{-0.06}$	$-0.13^{+0.06}_{-0.06}$	Yes	XRB	...

NOTE.—For the description of the Columns see Table 11.

^aWe do not have spectrum for this source (due to small number of counts) but its large errorbars at the color-color diagram place it on the region of candidate SNRs

TABLE 13
X-RAY COLORS FOR POTENTIAL SNRS IN NGC 4449

Source_ID	Col(S/M)	Col(M/H)	Col(S/H)	Spectra	Classification	Counterpart ^a
LZB_2	$0.27^{+0.08}_{-0.08}$	$0.74^{+0.16}_{-0.16}$	$1.00^{+0.16}_{-0.15}$	Yes	XRB	SNR/XRB
LZB_4	$-0.11^{+0.07}_{-0.07}$	$0.73^{+0.12}_{-0.11}$	$0.62^{+0.12}_{-0.11}$	Yes	XRB	SNR
LZB_5	$0.19^{+0.1}_{-0.78}$	$0.80^{+0.20}_{-0.18}$	$1.00^{+0.20}_{-0.18}$	Yes	XRB	SNR/XRB
LZB_8	$-0.14^{+0.05}_{-0.06}$	$0.89^{+0.12}_{-0.11}$	$0.75^{+0.12}_{-0.11}$	Yes	XRB	SNR/XRB
LZB_9	$0.25^{+0.13}_{-0.12}$	$0.93^{+0.39}_{-0.31}$	$1.18^{+0.38}_{-0.30}$	Yes	SNR	SNR/SSS
LZB_11	$-0.75^{+0.31}_{-0.39}$	$0.48^{+0.23}_{-0.21}$	$-0.27^{+0.36}_{-0.42}$	Yes	XRB	XRB
LZB_12	$-0.18^{+0.03}_{-0.03}$	$0.82^{+0.05}_{-0.05}$	$0.64^{+0.03}_{-0.05}$	Yes	SNR	SNR ^b
LZB_13	$2.25^{+0.43}_{-0.31}$	$0.63^{+1.06}_{-0.77}$	$2.89^{+0.95}_{-0.55}$	Yes	SSS	SSS
LZB_14	$1.47^{+0.72}_{-0.41}$	$0.37^{+1.15}_{-0.96}$	$1.88^{+0.95}_{-0.57}$	Yes	SSS	SSS
LZB_15	$-0.41^{+0.08}_{-0.08}$	$0.55^{+0.1}_{-0.07}$	$-0.04^{+0.09}_{-0.09}$	Yes	XRB	XRB
LZB_16	$0.01^{+0.02}_{-0.01}$	$0.99^{+0.06}_{-0.06}$	$0.99^{+0.05}_{-0.06}$	Yes	XRB	SNR/XRB
LZB_18	$-0.46^{+0.28}_{-0.33}$	$0.58^{+0.35}_{-0.31}$	$0.12^{+0.41}_{-0.41}$	Yes	unclassified	SNR/XRB
LZB_20	$0.37^{+0.52}_{-0.44}$	$-0.37^{+0.44}_{-0.52}$	$-0.01^{+0.35}_{-0.35}$	Yes	XRB	AGN
LZB_21	$-0.38^{+0.25}_{-0.27}$	$1.32^{+0.96}_{-0.57}$	$0.93^{+0.98}_{-0.61}$	Yes	unclassified	SNR/XRB
LZB_22	$0.95^{+0.98}_{-0.61}$	$-0.44^{+0.80}_{-1.07}$	$0.49^{+0.54}_{-0.43}$	Yes	foreground star	...
LZB_24	$0.63^{+0.69}_{-0.51}$	$0.38^{+1.15}_{-0.92}$	$1.04^{+0.98}_{-0.61}$	Yes	probable SNR	SNR/XRB ^c
LZB_25	$1.90^{+0.96}_{-0.55}$	$0.00^{+1.18}_{-1.18}$	$1.90^{+0.96}_{-0.55}$	Yes	SSS	SSS
LZB_26	$0.54^{+0.30}_{-0.27}$	$0.37^{+0.54}_{-0.46}$	$0.90^{+0.49}_{-0.38}$	Yes	probable SNR	SSS/XRB

NOTE.—For the description of the Columns see Table 11.

^aX-ray detected sources by Summers et al. (2003)

^bThe most oxygen rich SNR known (see §2.1)

^cIt is also detected in radio as HII region by Chomiuk & Wilcots (2009)

TABLE 14
X-RAY COLORS FOR POTENTIAL SNRS IN NGC 4214

Source_ID	Col(S/M)	Col(M/H)	Col(S/H)	Spectra	Classification	Counterpart
LZB_5	$0.65^{+0.44}_{-0.35}$	$-0.27^{+0.42}_{-0.48}$	$0.38^{+0.29}_{-0.26}$	Yes	XRB	...
LZB_7	$1.01^{+0.25}_{-0.21}$	$0.27^{+0.55}_{-0.44}$	$1.28^{+0.50}_{-0.33}$	Yes	SNR	...
LZB_10	$-0.21^{+0.32}_{-0.35}$	$0.61^{+0.69}_{-0.49}$	$0.40^{+0.73}_{-0.54}$	No	candidate SNR	Background galaxy ^d
LZB_11	$-0.35^{+0.36}_{-0.41}$	$1.03^{+0.98}_{-0.61}$	$0.66^{+1.03}_{-0.70}$	No	candidate SNR	...
LZB_16	$0.10^{+0.37}_{-0.36}$	$0.81^{+0.99}_{-0.64}$	$0.92^{+0.98}_{-0.63}$	No	candidate SNR	...
LZB_20	$-0.49^{+0.20}_{-0.22}$	$0.57^{+0.25}_{-0.21}$	$0.09^{+0.28}_{-0.28}$	Yes	XRB	...
LZB_23	$-0.55^{+0.34}_{-0.40}$	$0.81^{+0.70}_{-0.46}$	$0.26^{+0.80}_{-0.61}$	No	candidate SNR	...
LZB_24	$-0.24^{+0.05}_{-0.05}$	$0.34^{+0.05}_{-0.05}$	$0.08^{+0.07}_{-0.04}$	Yes	XRB	HII ^c
LZB_25	$-0.26^{+0.02}_{-0.02}$	$0.46^{+0.03}_{-0.03}$	$0.20^{+0.03}_{-0.03}$	Yes	XRB	...
LZB_26	$-0.42^{+0.05}_{-0.05}$	$0.58^{+0.06}_{-0.06}$	$0.15^{+0.07}_{-0.07}$	Yes	XRB	SNR/HII ^b
LZB_27	$0.11^{+0.20}_{-0.19}$	$1.25^{+0.96}_{-0.58}$	$1.38^{+0.95}_{-0.58}$	Yes	XRB	...
LZB_28	$-0.01^{+0.18}_{-0.18}$	$1.06^{+0.80}_{-0.47}$	$1.04^{+0.80}_{-0.47}$	Yes	probable SNR	SNR ^{a, b}
LZB_29	$-0.55^{+0.13}_{-0.14}$	$0.38^{+0.11}_{-0.11}$	$-0.18^{+0.15}_{-0.15}$	Yes	XRB	...
LZB_30	$0.95^{+0.28}_{-0.23}$	$0.89^{+0.99}_{-0.64}$	$1.85^{+0.96}_{-0.55}$	Yes	SNR	SNR ^b
LZB_31	$0.64^{+0.22}_{-0.20}$	$0.50^{+0.65}_{-0.45}$	$1.13^{+0.62}_{-0.38}$	Yes	probable SNR	...
LZB_33	$-0.77^{+0.15}_{-0.17}$	$0.30^{+0.10}_{-0.10}$	$-0.47^{+0.17}_{-0.18}$	Yes	XRB	...
LZB_34	$0.44^{+0.12}_{-0.12}$	$0.69^{+0.40}_{-0.29}$	$1.12^{+0.38}_{-0.27}$	Yes	probable SNR	SNR ^b
LZB_35	$0.23^{+0.13}_{-0.12}$	$1.13^{+0.81}_{-0.44}$	$1.36^{+0.81}_{-0.43}$	Yes	probable SNR	...
LZB_37	$-0.53^{+0.09}_{-0.09}$	$0.40^{+0.08}_{-0.07}$	$-0.13^{+0.10}_{-0.10}$	Yes	XRB	...
LZB_38	$0.66^{+0.49}_{-0.37}$	$0.60^{+1.09}_{-0.78}$	$1.29^{+0.96}_{-0.58}$	Yes	probable SNR	HII ^c
LZB_41	$0.98^{+0.99}_{-0.61}$	$-1.33^{+0.58}_{-0.96}$	$-0.34^{+0.25}_{-0.27}$	Yes	XRB	...
LZB_43	$-0.82^{+0.39}_{-0.60}$	$0.44^{+0.29}_{-0.25}$	$-0.38^{+0.49}_{-0.64}$	Yes	XRB	...

NOTE.—For the description of the Columns see Table 11. Sources 10, 11, 16 and 23 do not have adequate number of counts to allow us the extraction of their spectra, but their X-ray colors (within their errorbars) place them in the region of candidate SNRs.

^aRadio candidate SNR by Vukotić et al. (2005), the source is denoted as "q".

^bRadio candidate SNRs by Chomiuk & Wilcots (2009)

^cRadio classified HII regions by Chomiuk & Wilcots (2009)

^dThe classification criteria of Chomiuk & Wilcots (2009) for radio SNRs is the radio spectral index to be $\alpha \leq -0.2$ and H α emission associated with the source. In the case of this source, the radio spectral index is -0.32 but there is no detected H α emission, therefore they classify this source as a radio background galaxy.

TABLE 15
X-RAY COLORS FOR POTENTIAL SNRS IN NGC 2403

Source_ID	Col(S/M)	Col(M/H)	Col(S/H)	Spectra	Classification	Counterpart
LZB_2	$-0.26^{+0.11}_{-0.11}$	$0.79^{+0.23}_{-0.19}$	$0.54^{+0.24}_{-0.20}$	Yes	probable SNR	SNR (MFBL-29) ^a
LZB_5	$0.70^{+0.23}_{-0.19}$	$0.61^{+0.81}_{-0.49}$	$1.32^{+0.80}_{-0.41}$	Yes	probable SNR	...
LZB_14	$0.38^{+0.17}_{-0.16}$	$1.16^{+0.95}_{-0.54}$	$1.55^{+0.95}_{-0.52}$	Yes	probable SNR	SNR (MFBL-31,SP-30) ^b
LZB_21	$-0.26^{+0.06}_{-0.06}$	$0.55^{+0.13}_{-0.05}$	$0.30^{+0.09}_{-0.08}$	Yes	XRB	...
LZB_30	$0.28^{+0.16}_{-0.15}$	$1.35^{+0.95}_{-0.55}$	$1.62^{+0.95}_{-0.54}$	Yes	probable SNR	SNR (MFBL-7, Eck- μ ?)
LZB_39	$-0.35^{+0.11}_{-0.11}$	$0.48^{+0.13}_{-0.12}$	$0.13^{+0.14}_{-0.14}$	Yes	XRB	...
LZB_41	$0.62^{+0.16}_{-0.14}$	$0.55^{+0.47}_{-0.34}$	$1.17^{+0.45}_{-0.30}$	Yes	probable SNR	...
LZB_42	$0.18^{+0.12}_{-0.12}$	$1.21^{+0.83}_{-0.44}$	$1.39^{+0.83}_{-0.44}$	Yes	SNR	SNR (MFBL-17) ^c
LZB_54	$-0.74^{+0.09}_{-0.09}$	$0.32^{+0.07}_{-0.05}$	$-0.42^{+0.10}_{-0.10}$	Yes	XRB	...
LZB_58	$-0.78^{+0.15}_{-0.18}$	$0.18^{+0.11}_{-0.07}$	$-0.59^{+0.16}_{-0.18}$	Yes	XRB	...
LZB_63	$2.42^{+0.95}_{-0.55}$	$-0.23^{+1.10}_{-0.47}$	$2.14^{+0.89}_{-0.47}$	Yes	SSS	...
LZB_64	$-0.04^{+0.04}_{-0.04}$	$0.62^{+0.08}_{-0.06}$	$0.57^{+0.06}_{-0.06}$	Yes	XRB	...
LZB_65	$-0.19^{+0.08}_{-0.07}$	$0.50^{+0.10}_{-0.10}$	$0.32^{+0.11}_{-0.10}$	Yes	XRB	...
LZB_68	$1.01^{+0.72}_{-0.44}$	$0.045^{+1.01}_{-0.93}$	$1.06^{+0.81}_{-0.47}$	Yes	probable SNR	...
LZB_69	$-0.16^{+0.03}_{-0.03}$	$0.48^{+0.04}_{-0.04}$	$0.32^{+0.05}_{-0.04}$	Yes	XRB	...
LZB_71	$1.90^{+0.35}_{-0.24}$	$0.07^{+0.60}_{-0.53}$	$1.98^{+0.48}_{-0.30}$	Yes	probable SNR	SNR (MFBL-33 ?)
LZB_72	$2.26^{+0.93}_{-0.52}$	$-0.23^{+1.09}_{-1.15}$	$1.97^{+0.90}_{-0.44}$	Yes	SSS	...
LZB_75	$0.59^{+0.32}_{-0.27}$	$0.17^{+0.57}_{-0.49}$	$0.75^{+0.51}_{-0.35}$	Yes	XRB	...
LZB_76	$0.34^{+0.19}_{-0.18}$	$1.24^{+0.96}_{-0.58}$	$1.59^{+0.95}_{-0.57}$	Yes	probable SNR	...
LZB_78	$0.47^{+0.11}_{-0.10}$	$1.09^{+0.77}_{-0.41}$	$1.55^{+0.77}_{-0.40}$	Yes	probable SNR	...
LZB_80	$0.56^{+0.26}_{-0.22}$	$0.55^{+0.83}_{-0.52}$	$1.10^{+0.81}_{-0.43}$	Yes	probable SNR	SNR (MFBL-24)
LZB_81	$0.49^{+0.16}_{-0.15}$	$1.09^{+0.92}_{-0.51}$	$1.59^{+0.90}_{-0.49}$	Yes	SNR	...
LZB_86	$0.66^{+0.33}_{-0.27}$	$0.16^{+0.59}_{-0.50}$	$0.82^{+0.51}_{-0.35}$	Yes	probable SNR	SNR (MFBL-22)
LZB_93	$0.13^{+0.05}_{-0.05}$	$0.49^{+0.08}_{-0.08}$	$0.63^{+0.09}_{-0.07}$	Yes	XRB	SNR (MFBL-18 ?)
LZB_98	$-0.52^{+0.04}_{-0.05}$	$0.37^{+0.05}_{-0.04}$	$-0.14^{+0.05}_{-0.06}$	Yes	XRB	...
LZB_99	$-0.85^{+0.04}_{-0.05}$	$0.35^{+0.03}_{-0.02}$	$-0.50^{+0.04}_{-0.04}$	Yes	XRB	SNR (MFBL-30)
LZB_100	$-0.67^{+0.07}_{-0.04}$	$0.06^{+0.11}_{-0.03}$	$-0.60^{+0.06}_{-0.05}$	Yes	XRB	...
LZB_101	$0.01^{+0.04}_{-0.04}$	$0.34^{+0.06}_{-0.05}$	$0.35^{+0.06}_{-0.05}$	Yes	XRB	...
LZB_103	$-0.46^{+0.01}_{-0.01}$	$0.27^{+0.01}_{-0.01}$	$-0.20^{+0.02}_{-0.02}$	Yes	XRB	XRB, ULX ^d
LZB_104	$-0.44^{+0.01}_{-0.01}$	$0.44^{+0.01}_{-0.01}$	$-0.01^{+0.002}_{-0.01}$	Yes	XRB	SNR (MFBL-15) ^e
LZB_105	$-0.33^{+0.04}_{-0.04}$	$0.65^{+0.05}_{-0.05}$	$0.33^{+0.05}_{-0.06}$	Yes	XRB	ULX ^f
LZB_107	$0.34^{+0.04}_{-0.03}$	$2.27^{+0.92}_{-0.44}$	$2.59^{+0.92}_{-0.44}$	Yes	SNR	SNR (TH-2) ^g
LZB_109	$-0.57^{+0.01}_{-0.01}$	$0.48^{+0.01}_{-0.01}$	$-0.09^{+0.01}_{-0.01}$	Yes	XRB	ULX ^h
LZB_112	$-0.39^{+0.05}_{-0.05}$	$0.42^{+0.05}_{-0.05}$	$0.04^{+0.04}_{-0.01}$	Yes	XRB	...
LZB_115	$-0.30^{+0.08}_{-0.09}$	$0.29^{+0.09}_{-0.08}$	$-0.01^{+0.10}_{-0.10}$	Yes	XRB	...
LZB_120	$-0.16^{+0.06}_{-0.06}$	$0.42^{+0.09}_{-0.07}$	$0.26^{+0.10}_{-0.08}$	Yes	probable SNR	...

NOTE.—For the description of the Columns see Table 11.

NOTE.—(MFBL): Optically identified SNRs by Matonick et al. (1997); (SP): X-ray identified SNRs by Schlegel & Pannuti (2003); (TH): Radio candidate SNR by Turner & Ho (1994); (Eck): Radio candidate SNR by Eck et al. (2002). The questionmarks correspond to large position offsets.

^aThis source is also X-ray detected (SP-31) by Schlegel & Pannuti (2003).

^bAlso X-ray detected by Pannuti et al. (2007).

^cThis source is also X-ray detected (SP-16) by Schlegel & Pannuti (2003) and Pannuti et al. (2007).

^dXRB by Schlegel & Pannuti (2003) while it is also detected as ULX by Winter et al. (2006)

^eSchlegel & Pannuti (2003) have extracted spectra for this source (SP20) without defining any classification. Also detected as ULX by Winter et al. (2006)

^fWinter et al. (2006).

^gAlso X-ray detected (SP-12) by Schlegel & Pannuti (2003) and Pannuti et al. (2007).

^hClassified as ULX by Winter et al. (2006) and Schlegel & Pannuti (2003).

TABLE 16
X-RAY COLORS FOR POTENTIAL SNRS IN NGC 5204

Source_ID	Col(S/M)	Col(M/H)	Col(S/H)	Spectra	Classification	Counterpart
LZB_8	$0.30^{+0.08}_{-0.08}$	$0.80^{+0.20}_{-0.20}$	$1.1^{+0.20}_{-0.20}$	Yes	XRБ	...
LZB_10	$0.03^{+0.005}_{-0.005}$	$0.79^{+0.01}_{-0.01}$	$0.82^{+0.01}_{-0.01}$	Yes	XRБ	...
LZB_11	$-0.16^{+0.06}_{-0.06}$	$0.36^{+0.07}_{-0.07}$	$0.22^{+0.07}_{-0.10}$	Yes	XRБ	...

NOTE.—For the description of the Columns see Table 11.

TABLE 17
SPECTRAL FITTING RESULTS OF THE POINT-SOURCES IN NGC 3077

Source_ID	Model	N_{H} ($\times 10^{22} \text{ cm}^{-2}$)	Γ/kT (Index/keV)	Norm (10^{-5} A)	χ^2/dof or Cstat	Goodness(%) (for Cstat)	F_{abs} ($\times 10^{-15} \text{ erg s}^{-1} \text{ cm}^{-1}$)	F_{unabs} ($\text{erg s}^{-1} \text{ cm}^{-1}$)	$\log L_X^{\text{unabs}}$ (erg s^{-1})	Classification
chi-square statistics										
LZB_15	apec	$0.06^{+0.05}_{-0.04}$	$2.8^{+1.18}_{-0.68}$	$1.5^{+0.25}_{-0.26}$	4.98/10	...	21	24	37.6	probable SNR
LZB_19	PL	$0.14^{+0.13}_{-0.12}$	$1.38^{+0.31}_{-0.19}$	$0.32^{+0.21}_{-0.12}$	4.15/6	..	7.9	58	38.0	XRB
cash statistics										
LZB_2	bbody	$0.41^{+0.14}_{-0.12}$	$0.02^{+0.09}_{-0.01}$	> 936.2	1.84	56.0	3.2	5500	39.9	SSS ^b
LZB_6	apec	$0.34^{+0.43}_{-0.34}$	$0.30^{+0.45}_{-0.22}$	> 0.44	0.56	46.9	1.5	8.3	37.1	probable SNR ^b
LZB_8	PL	0.05^{a}	$3.29^{+2.32}_{-2.09}$	$0.02^{+0.02}_{-0.02}$	2.48	20.5	0.8	1.2	36.3	XRB
LZB_12	apec	$0.70^{+0.53}_{-0.70}$	0.77 (> 0.18)	$0.18^{+2.8}_{-0.18}$	3.54	46.6	0.8	4.6	36.8	probable SNR
LZB_13	apec	$2.97^{+4.8}_{-1.4}$	$0.19^{+0.43}_{-0.19}$	> 111.1	1.44	78.3	0.7	1800	39.4	probable SNR
LZB_14	PL	0.05^{a}	$1.35^{+0.76}_{-0.76}$	$0.06^{+0.03}_{-0.002}$	2.22	11.1	5.9	6.3	36.8	XRB
LZB_18	apec	$0.99^{+0.16}_{-0.16}$	$0.75^{+0.08}_{-0.13}$	$3.13^{+2.0}_{-0.95}$	109.4	96	9.3	82.3	38.1	probable SNR ^{b, c}

NOTE.—Column 1: Source ID; Column 2: Fitted model; Column 3: $H\text{I}$ Column Density; Column 4: Best fit value of the power law photon index or the thermal component temperature in keV; Column 5: The normalization factor given in units of 10^{-5} K . For apec A is: $10^{-14} (4\pi D_A^2)^{-1} \int n_e n_p dV$, where D_A is the angular distance to the source in centimeters and $n_e n_p$ are the electron and proton densities respectively in cm^{-2} , for PL: photons $\text{keV}^{-1} \text{ cm}^{-2}$ at 1 keV and for bbody: $10^{39} \text{ erg s}^{-1} (10 \text{ kpc})^{-1}$; Column 6: $\chi^2/\text{degrees of freedom}$ or Cash statistic; Column 7: Goodness-of fit for Cash statistics; Column 8: Absorbed flux in 0.3 - 10 keV band; Column 9: Unabsorbed flux in 0.3 - 10 keV band; Column 10: Source classification

^aFixed to Galactic line-of-sight value

^bOtt et al. (2003) have classified our LZB6, LZB18 as X-ray SNRs and LZB2 as a SSS

^cRadio candidate SNR by Rosa-González (2005)

TABLE 18
SPECTRAL FITTING RESULTS OF THE POINT-SOURCES IN NGC 4395

Source	Model	N_{H} ($\times 10^{22} \text{ cm}^{-2}$)	Γ/kT (Index/keV)	Norm (10^{-5} A)	χ^2/dof or Cstat	Goodness(%) (for Cstat)	F_{abs} ($\times 10^{-14}$)	F_{unabs} ($\text{erg s}^{-1} \text{ cm}^{-1}$)	$\log L_{\text{X}}^{\text{unabs}}$ (erg s^{-1})	Classification
chi-square statistics										
LZB_14	apec + apec	0.545	1.37	94	8.65/4	...	3.1	75.4	38.8	SNR
...	0.17	10.1	37.8	...
LZB_15	PL	$0.03^{+0.06}_{-0.03}$	$1.37^{+0.32}_{-0.25}$	$1.27^{+0.48}_{-0.26}$	16.25/13	...	12	12	38.0	XRB
cash statistics										
LZB_1	PL	0.0185 ^a	$0.64^{+1.46}_{-3.64}$	$0.30^{+0.27}_{-0.15}$	3.62	60.0	7.9	8.0	37.8	XRB
LZB_2	PL	$0.03^{+0.19}_{-0.03}$	$3.36^{+3.13}_{-1.70}$	$0.33^{+0.46}_{-0.33}$	2.74	21.1	1.5	2.0	37.2	XRB
LZB_5	PL	0.0185 ^a	$2.14^{+0.59}_{-0.58}$	$0.24^{+0.08}_{-0.06}$	2.78	7.3	1.2	1.3	37.0	XRB
LZB_6	PL	0.0185 ^a	$1.27^{+1.26}_{-1.26}$	$0.05^{+0.04}_{-0.05}$	9.75	84.4	0.6	0.6	36.7	XRB
LZB_7	PL	0.0185 ^a	$2.06^{+4.30}_{-5.06}$	$0.05^{+0.06}_{-0.05}$	4.13	74.2	0.3	0.3	36.4	XRB
LZB_12	PL	0.0185 ^a	$1.61^{+0.34}_{-0.34}$	$0.51^{+0.10}_{-0.09}$	27.0	6.0	3.7	3.8	37.5	XRB

NOTE.—For the description of the Columns see Table 17.

^aFixed to Galactic line-of-sight value

TABLE 19
SPECTRAL FITTING RESULTS OF THE POINT-SOURCES IN NGC 4449

Source	Model	N_{H} ($\times 10^{22} \text{ cm}^{-2}$)	Γ/kT (Index/keV)	Norm (10^{-5} A)	χ^2/dof or Cstat	Goodness(%) (for Cstat)	F_{abs} ($\times 10^{-14}$)	F_{unabs} $\text{erg s}^{-1} \text{ cm}^{-1}$)	$\log L_{\text{X}}^{\text{unabs}}$ (erg s^{-1})	Classification ^a
chi-square statistics										
LZB_2	PL	$0.03^{+0.11}_{-0.03}$	$2.46^{+1.37}_{-0.48}$	$0.61^{+0.55}_{-0.14}$	7.43/6	...	2.5	3.0	37.8	XRB
...	$kT=1.25^{+0.90}_{-0.32}$	> 0.13
LZB_8	PL	$0.20^{+0.15}_{-0.09}$	$2.48^{+0.49}_{-0.53}$	$1.94^{+1.58}_{-0.82}$	1.45/6	...	5.0	9.4	38.3	XRB
LZB_12	PL + 2apec	$0.30^{+0.44}_{-0.09}$	$\Gamma = 1.67^{+0.21}_{-0.75}$	$1.62^{+1.47}_{-1.46}$	26.7/27	...	18	41	38.9	SNR ^c
...	$kT_1 = 0.25^{+0.09}_{-0.11}$	> 2.80
...	$kT_2 = 1.27^{+0.09}_{-0.11}$	$8.00^{+7.00}_{-2.50}$
LZB_13	bbody	$0.01^{+0.07}_{-0.01}$	$0.09^{+0.01}_{-0.01}$	$0.15^{+0.22}_{-0.04}$	18.7/16	...	6.3	7.5	38.2	SSS
LZB_16	PL	$0.07^{+0.04}_{-0.03}$	$2.13^{+0.24}_{-0.2}$	$5.76^{+1.01}_{-0.79}$	53.9/36	...	24	30	38.8	XRB
cash statistics										
LZB_4	PL + apec	$0.08^{+0.12}_{-0.08}$	$\Gamma = 1.81^{+0.67}_{-0.63}$	$0.66^{+0.54}_{-0.30}$	78.5	2.0	4.2	4.9	38.0	XRB
...	$kT=1.08^{+0.26}_{-0.28}$	$0.34^{+0.31}_{-0.21}$
LZB_5	PL	0.0161^{b}	$2.3^{+0.27}_{-0.27}$	$0.44^{+0.06}_{-0.07}$	75.2	30.0	2.1	2.2	37.7	XRB
LZB_9	apec	0.0161^{b}	$0.99^{+1.10}_{-0.26}$	$0.32^{+0.37}_{-0.07}$	19.9	93.6	0.7	0.7	37.2	SNR
LZB_11	PL	$0.31^{+0.65}_{-0.31}$	$1.5^{+1.80}_{-1.40}$	$0.18^{+0.07}_{-0.18}$	0.7	30.5	1.2	1.5	37.5	XRB
LZB_14	bbody	0.0161^{b}	$0.06^{+0.02}_{-0.02}$	$0.04^{+0.12}_{-0.02}$	6.7	68.3	0.9	1.1	37.4	SSS
LZB_15	PL	$0.16^{+0.10}_{-0.10}$	$1.6^{+0.37}_{-0.36}$	$1.06^{+0.47}_{-0.30}$	113.6	6.0	6.6	8.0	38.2	XRB
LZB_18	PL	$0.56^{+1.15}_{-0.56}$	$3.04^{+3.09}_{-1.92}$	$0.28^{+3.70}_{-0.28}$	9.8	87.0	0.3	1.5	37.5	unclassified
...	apec	$1.15^{+0.72}_{-1.15}$	> 0.36	$0.73^{+6.38}_{-0.73}$	9.8	87.4	0.2	1.7	37.6	...
LZB_20	PL	0.0161^{b}	$1.37^{+1.21}_{-1.06}$	$0.03^{+0.03}_{-0.03}$	10.2	91.3	0.3	0.3	36.7	XRB
LZB_21	PL	$0.02^{+1.33}_{-0.02}$	$0.99^{+6.84}_{-1.47}$	$0.08^{+1.55}_{-0.04}$	2.4	41.8	1.2	1.2	37.4	unclassified
...	apec	$1.24^{+0.54}_{-0.66}$	$0.23^{+0.56}_{-0.09}$	> 13.0	5.4	71.8	0.2	24	38.7	...
LZB_22	apec	$0.53^{+0.45}_{-0.51}$	$0.11^{+0.10}_{-0.06}$	> 23.9	3.8	73.6	0.1	15	38.5	foreground star
LZB_24	apec	0.0161^{b}	$0.23^{+0.11}_{-0.08}$	$0.07^{+0.13}_{-0.07}$	4.3	35.0	0.1	0.1	36.4	probable SNR ^d
LZB_25	bbody	$0.44^{+3.25}_{-0.13}$	$0.04^{+0.03}_{-0.02}$	> 84.8	5.8	95.6	0.5	220	39.7	SSS
LZB_26	apec	0.0161^{b}	$1.02^{+0.84}_{-0.30}$	$0.09^{+0.11}_{-0.04}$	13.3	91.5	0.2	0.4	36.9	probable SNR

NOTE.—For the description of the Columns see Table 17.

^aAlready X-ray detected sources by Summers et al. (2003)

^bFixed to Galactic line-of-sight value

^cOxygen rich SNR detected in all bands

^dRadio observations by Chomiuk & Wilcots (2009) denote this source as an HII region.

TABLE 20
SPECTRAL FITTING RESULTS OF THE POINT-SOURCES IN NGC 4214

Source	Model	N_H ($\times 10^{22} \text{ cm}^{-2}$)	Γ/kT (Index/keV)	Norm (10^{-5} A)	χ^2/dof or Cstat	Goodness(%) (for Cstat)	F_{abs} ($\times 10^{-15}$)	F_{unabs} ($\text{erg s}^{-1} \text{ cm}^{-1}$)	$\log L_X^{unabs}$ (erg s^{-1})	Classification
chi-square statistics										
LZB_24 (2030)	PL+apec	$0.28^{+0.30}_{-0.10}$	$\Gamma = 1.69^{+0.41}_{-0.18}$	$1.30^{+0.76}_{-0.48}$	31.07/23	...	72	130	38.5	XRB ^c
...	$\text{kT}=0.18^{+0.08}_{-0.05}$	$2.50^{+58.6}_{-2.34}$
(4793)	0.575	42	75	38.3	...
(5197)	0.488	35	64	38.2	...
LZB_25 (2030)	PL	$0.12^{+0.02}_{-0.02}$	$1.68^{+0.13}_{-0.12}$	$4.90^{+0.68}_{-0.59}$	105.5/66	...	290	340	38.9	XRB
(4793)	0.192	55	66	38.2	...
(5197)	0.904	260	310	38.9	...
LZB_26 (2030)	PL	$0.27^{+0.07}_{-0.09}$	$2.15^{+0.50}_{-0.40}$	$0.84^{+0.53}_{-0.30}$	12.4/11	...	43.8	25.9	37.8	XRB ^e
(4793)	1.950	84.5	50.0	38.1	...
(5197)	1.660	71.1	42.1	38.0	...
cash statistics										
LZB_5 (2030)	PL	0.0199 ^d	$0.99^{+1.09}_{-1.04}$	$0.16^{+0.18}_{-0.16}$	19.8	96.5	24	25	37.8	XRB
(5197)	0.15	3.7	3.7	37.0	...
LZB_7 (2030)	apec	0.0199 ^d	$0.28^{+0.04}_{-0.04}$	$0.18^{+0.08}_{-0.05}$	15.8	81.8	2.9	3.3	36.9	SNR
(4793)	0.85	2.5	2.8	36.9	...
(5197)	0.95	2.8	3.2	36.9	...
LZB_20 (2030)	PL	$0.47^{+1.00}_{-0.47}$	$2.88^{+3.90}_{-2.62}$	> 0.49	4.16	66.3	6.5	24.6	37.8	XRB
LZB_27 (2030)	PL	0.0199 ^d	$2.64^{+0.94}_{-0.90}$	$0.04^{+0.03}_{-0.02}$	23.4	85.8	1.8	2.0	36.7	XRB
(4793)	0.87	1.6	1.8	36.7	...
(5197)	0.83	1.5	1.7	36.6	...
LZB_28(2030)	apec	$0.68^{+0.37}_{-0.37}$	$0.25^{+0.29}_{-0.10}$	> 1.30	36.0	99.5	0.8	24	37.8	probable SNR ^{a, b}
(4793)	1.70	1.4	40	38.0	...
(5197)	1.44	1.2	34	37.9	...
LZB_29 (2030)	PL	$0.18^{+0.32}_{-0.18}$	$1.55^{+1.00}_{-0.82}$	$0.16^{+0.16}_{-0.24}$	9.29	26.0	10	12	37.5	XRB
(4793)	1.37	14	17	37.6	...
(5197)	1.08	11	13	37.5	...
LZB_30 (2030)	apec	0.0199 ^d	$0.29^{+0.05}_{-0.05}$	$0.12^{+0.06}_{-0.05}$	12.2	15.0	1.9	2.2	36.8	SNR ^b
(4793)	0.99	1.9	2.2	36.8	...
(5197)	1.32	2.5	2.9	36.9	...
LZB_31 (2030)	apec	0.0199 ^d	$0.36^{+0.13}_{-0.07}$	$0.10^{+0.06}_{-0.04}$	37.9	92.2	1.8	2.1	36.7	probable SNR
(4793)	0.73	1.3	1.5	36.6	...
(5197)	0.75	1.4	1.5	36.6	...
LZB_33 (2030)	PL	$0.37^{+0.36}_{-0.33}$	$1.21^{+0.78}_{-0.78}$	$0.12^{+0.16}_{-0.12}$	12.3	28.5	12	14	37.6	XRB
(4793)	2.26	26	31	37.9	...
(5197)	2.32	27	32	37.9	...
LZB_34 (2030)	apec	$0.66^{+0.10}_{-0.19}$	$0.14^{+0.05}_{-0.05}$	> 37.1	14.4	72.0	3.2	410	39.0	probable SNR ^b
(4793)	0.63	2.0	260	38.8	...
(5197)	1.44	4.6	590	39.2	...
LZB_35 (2030)	apec	0.0199 ^d	$0.75^{+0.16}_{-0.18}$	$0.16^{+0.05}_{-0.05}$	10.58	57	3.9	4.3	37.0	probable SNR

TABLE 20—*Continued*

Source	Model	N_{H} ($\times 10^{22} \text{ cm}^{-2}$)	Γ/kT (Index/keV)	Norm (10^{-5} A)	χ^2/dof or Cstat	Goodness(%) (for Cstat)	F_{abs} ($\times 10^{-15} \text{ erg s}^{-1} \text{ cm}^{-1}$)	F_{unabs} ($\text{erg s}^{-1} \text{ cm}^{-1}$)	$\log L_{\text{X}}^{\text{unabs}}$ (erg s^{-1})	Classification
(4793)	0.44	1.7	1.8	36.7	...
(5197)	0.33	1.3	1.4	36.6	...
LZB_37 (2030)	PL	$0.20^{+0.14}_{-0.12}$	$1.68^{+0.46}_{-0.42}$	$0.44^{+0.25}_{-0.16}$	32.7	53.7	24	31	37.9	XRB
(4793)	1.01	24	31	37.9	...
(5197)	1.01	24	31	37.9	...
LZB_38 (2030)	apec	0.0199 ^d	$0.20^{+0.12}_{-0.08}$	$0.05^{+0.10}_{-0.05}$	15.6	96	0.7	0.9	36.4	probable SNR ^c
(4743)	1.68	1.2	1.5	36.6	...
LZB_41 (2030)	PL	0.0199 ^d	$0.54^{+0.82}_{-0.83}$	$0.02^{+0.02}_{-0.02}$	32.8	100	5.4	5.4	37.2	XRB
(5197)	1.00	5.4	5.4	37.2	...
LZB_43 (2030)	PL	0.0199 ^d	$1.43^{+0.77}_{-0.76}$	$0.03^{+0.04}_{-0.03}$	28.3	97.7	2.6	2.6	36.8	XRB
(4793)	1.31	3.4	3.5	37.0	...
(5197)	1.23	3.2	3.3	36.9	...

NOTE.—Description of columns: Column 1: Source ID. The numbers in parenthesis show the observation ID used, Column 2: Fitted model, Column 3: HI column Density, Column 4: Best fit value of the power law photon index or the thermal component temperature in keV, Column 5: Model normalization for the first observation used. In the case of multiple observations the number presented in column 5 is the conversion factor which is multiplied to the model normalization. The latter is given in units of 10^{-5} K , where K is for apec: $10^{-14} (4\pi D_A^2)^{-1} \int n_e n_p dV$; D_A is the angular distance to the source in centimeters and $n_e n_p$ are the electron and proton densities respectively in cm^{-2} , for PL: photons $\text{keV}^{-1} \text{ cm}^{-2}$ at 1 keV and for bbody: $10^{39} \text{ erg s}^{-1} (10 \text{ kpc})^{-1}$, Column 6: $\chi^2/\text{degrees of freedom}$ or Cash statistic, Column 7: Goodness-of fit for Cash statistics, Column 8: Absorbed flux in 0.3 - 10 keV band, Column 9: Unabsorbed flux in 0.3 - 10 keV band, Column 10: Source classification

^aRadio candidate SNR by Vukotić et al. (2005)

^bRadio candidate SNR by Chomiuk & Wilcots (2009)

^cRadio classified HII regions by Chomiuk & Wilcots (2009)

^dFixed to Galactic line-of-sight value

^eRadio SNR/HII detected by Chomiuk & Wilcots (2009)

TABLE 21
SPECTRAL FITTING RESULTS OF THE SNR CANDIDATES IN NGC 2403

Source	Model	N_H ($\times 10^{22} \text{ cm}^{-2}$)	Γ/kT (Index/keV)	Norm (10^{-5} A)	χ^2/dof or Cstat	Goodness(%) (for Cstat)	F_{abs} ($\times 10^{-15} \text{ erg s}^{-1} \text{ cm}^{-1}$)	F_{unabs} ($\text{erg s}^{-1} \text{ cm}^{-1}$)	$\log L_X^{unabs}$ (erg s^{-1})	Classification
chi-square statistics										
LZB_21 (4630)	PL	$0.14^{+0.07}_{-0.08}$	$2.06^{+0.20}_{-0.40}$	$1.02^{+0.40}_{-0.28}$	8.3/14	...	40	55	37.8	XRB
LZB_54 (4628)	PL	$0.25^{+0.22}_{-0.15}$	$1.37^{+0.32}_{-0.40}$	$0.23^{+0.14}_{-0.15}$	16.2/11	...	18	22	37.4	XRB
(4629)	PL	1.16	21	25	37.5	...
(4630)	PL	1.50	28	33	37.6	...
LZB_58 (4630)	PL	$0.12^{+0.31}_{-0.12}$	$1.32^{+0.54}_{-0.40}$	$0.38^{+0.35}_{-0.14}$	4.77/5	...	35	39	37.7	XRB
LZB_64 (2014)	PL + apec	0.0436^d	$\Gamma = 1.95^{+0.23}_{-0.26}$	$0.56^{+0.09}_{-0.12}$	40.99/33	...	34	39	37.7	XRB
...	$kT=0.82^{+0.16}_{-0.11}$	$0.26^{+0.09}_{-0.09}$
(4630)	2.06	71	80	38.0	...
LZB69 (4628)	PL	$0.08^{+0.03}_{-0.04}$	$1.89^{+0.11}_{-0.16}$	$1.00^{+0.21}_{-0.17}$	44.9/56	...	49	60	37.9	XRB
(4629)	1.26	63	76	38.0	...
(4630)	1.93	46	56	37.8	...
LZB_71 (4629)	apec+apec	4.24	$kT_1=1.72$	5.60	29.1/13	...	79	92	38.0	probable SNR ^a
...	$kT_2=0.10$	1.04
(4630)	0.79	63	73	37.9	...
LZB_93 (4628)	PL	0.0436^d	$2.48^{+0.22}_{-0.22}$	> 0.37	12.4/14	...	20	25	37.5	XRB ^a
(4630)	0.79	11	14	37.2	...
LZB_98 (2014)	PL	$0.26^{+0.10}_{-0.06}$	$1.63^{+0.17}_{-0.21}$	$0.59^{+0.19}_{-0.14}$	55.52/35	...	34	44	37.7	XRB
(4628)	0.90	30	39	37.7	...
(4629)	1.20	41	53	37.8	...
(4630)	1.00	34	44	37.7	...
LZB_99 (2014)	PL + apec	$0.66^{+0.27}_{-0.12}$	$\Gamma = 1.94^{+0.18}_{-0.16}$	$2.67^{+0.68}_{-0.65}$	72.24/83	...	94	180	38.3	XRB ^a
...	$kT=1.02^{+0.34}_{-0.45}$	$1.12^{+1.29}_{-0.64}$
(4628)	0.47	44	85	38.0	...
(4629)	0.88	82	160	38.3	...
(4630)	1.04	97	190	38.4	...
LZB_100 (4628)	PL	$0.18^{+0.07}_{-0.06}$	$0.88^{+0.13}_{-0.13}$	$1.5^{+0.3}_{-0.2}$	47.59/50	...	258	275	38.5	XRB
(4629)	0.20	52	56	37.8	...
LZB_101 (4629)	PL + apec	0.0436^d	$\Gamma = 1.64^{+0.27}_{-0.22}$	$0.89^{+0.20}_{-0.19}$	30.46/22	...	67	720	38.9	XRB
...	$kT=0.34^{+0.25}_{-0.07}$	$0.41^{+0.21}_{-0.26}$
LZB_103 (2014)	PL	$0.13^{+0.02}_{-0.02}$	$1.45^{+0.06}_{-0.06}$	$5.98^{+0.47}_{-0.44}$	354.5/317	...	460	530	38.8	XRB
(4628)	0.77	360	410	38.7	...
(4629)	0.86	390	450	38.7	...
(4630)	0.82	380	430	38.7	...
LZB_104 (2014)	PL	$0.26^{+0.02}_{-0.02}$	$1.91^{+0.05}_{-0.05}$	$14.6^{+0.86}_{-0.80}$	600/534	...	590	870	39.0	XRB ^a
(4628)	0.77	460	670	38.9	...
(4629)	0.86	510	740	39.0	...
(4630)	0.86	510	740	39.0	...
LZB_105 (4629)	PL	$0.17^{+0.04}_{-0.05}$	$2.28^{+0.14}_{-0.19}$	$1.5^{+0.38}_{-0.30}$	48.6/42	...	47	76	38.0	XRB
(4630)	1.52	71	110	38.1	...
LZB_107 (2014)	2×apec	$0.09^{+0.10}_{-0.06}$	$kT_1=0.80^{+0.12}_{-0.09}$	$2.04^{+1.28}_{-0.92}$	50.54/40	...	19	33	37.6	SNR ^b
...	$kT_2=0.27^{+0.06}_{-0.06}$	$2.99^{+5.04}_{-1.79}$

TABLE 21—*Continued*

Source	Model	N_{H} ($\times 10^{22} \text{ cm}^{-2}$)	Γ/kT (Index/keV)	Norm (10^{-5} A)	χ^2/dof or Cstat	Goodness(%) (for Cstat)	F_{abs} ($\times 10^{-15} \text{ erg s}^{-1} \text{ cm}^{-1}$)	F_{unabs}	$\log L_{\text{X}}^{\text{unabs}}$ (erg s^{-1})	Classification
(4628)	0.91	18	30	37.6	...
(4629)	1.15	23	38	37.7	...
(4630)	0.98	19	32	37.6	...
LZB_109 (2014)	PL	$0.39^{+0.01}_{-0.01}$	$2.30^{+0.04}_{-0.04}$	$44.5^{+2.14}_{-1.93}$	695.1/568	...	1100	2200	39.4	XRБ
(4628)	1.22	1300	2700	39.5	...
(4630)	0.94	1000	2100	39.4	...
LZB_112 (2014)	PL	$0.05^{+0.06}_{-0.05}$	$1.61^{+0.21}_{-0.30}$	$0.82^{+0.29}_{-0.19}$	17.22/20	...	56	62	37.9	XRБ
(4629)	0.47	27	29	37.6	...
(4630)	0.30	17	19	37.4	...
LZB_115 (2014)	PL	0.0436 ^d	$1.28^{+0.28}_{-0.28}$	$0.45^{+0.07}_{-0.08}$	15.5/8	...	46	48	37.8	XRБ
LZB_120 (4628)	apec	0.0436 ^d	$2.75^{+1.54}_{-0.70}$	$1.03^{+0.18}_{-0.18}$	18.8/12	...	15	16	37.3	probable SNR
(4629)	0.83	12	14	37.2	...
cash statistics										
LZB_2 (4628)	apec	0.0436 ^d	$2.98^{+6.50}_{-1.27}$	$0.13^{+0.07}_{-0.05}$	36.8	89	1.9	2.0	36.4	probable SNR ^a
(4629)	1.6	3.0	3.3	36.6	...
(4630)	1.7	3.2	3.4	36.6	...
LZB_5 (2014)	apec	0.0436 ^d	$0.28^{+0.05}_{-0.03}$	$0.09^{+0.05}_{-0.04}$	30.1	97.6	1.2	1.8	36.3	probable SNR
(4628)	0.97	1.2	1.7	36.3	...
(4629)	0.94	1.2	1.6	36.3	...
(4630)	1.21	1.5	2.1	36.4	...
LZB_14 (2014)	apec	0.0436 ^d	$0.29^{+0.07}_{-0.06}$	$0.12^{+0.06}_{-0.04}$	29.5	94	1.7	2.3	36.4	probable SNR ^a
(4628)	0.31	0.5	0.7	35.9	...
(4629)	0.80	1.4	1.8	36.3	...
(4630)	0.37	0.6	0.8	36.0	...
LZB_30 (2014)	apec	$0.48^{+0.14}_{-0.30}$	$0.18^{+0.08}_{-0.04}$	$2.12^{+9.86}_{-2.12}$	30.7	91.6	1.2	33	37.6	probable SNR ^{a, c}
(4628)	1.07	1.2	35	37.6	...
(4629)	1.25	1.4	41	37.7	...
(4630)	0.69	0.8	23	37.4	...
LZB_39 (2014)	PL	$0.15^{+0.20}_{-0.15}$	$1.83^{+0.62}_{-0.56}$	$0.20^{+0.17}_{-0.09}$	31.05	10	9.9	12.8	37.2	XRБ
(4628)	0.35	3.5	4.5	36.7	...
(4630)	0.75	7.5	9.7	37.1	...
LZB_41 (2014)	apec	0.0436 ^d	$0.25^{+0.03}_{-0.02}$	$0.08^{+0.05}_{-0.03}$	44.9	95.3	1.1	1.5	36.3	probable SNR
(4628)	0.84	0.9	1.3	36.2	...
(4629)	1.79	1.9	2.7	36.5	...
(4630)	1.68	1.8	2.6	36.5	...
LZB_42 (2014)	apec	0.0436 ^d	$0.77^{+0.21}_{-0.21}$	$0.07^{+0.03}_{-0.02}$	32.3	67.8	1.5	1.8	36.3	SNR ^a
(4628)	1.00	1.6	1.8	36.3	...
(4629)	0.86	1.3	1.6	36.3	...
(4630)	0.65	1.0	1.2	36.2	...
LZB_63 (4629)	bbody	0.0436 ^d	$0.06^{+0.01}_{-0.01}$	$10.2^{+17.7}_{-0.04}$	18.7	39	1.4	2.6	37.5	SSS
LZB_65 (4628)	PL	0.0436 ^d	$1.73^{+0.25}_{-0.25}$	$0.16^{+0.05}_{-0.04}$	25.6	25	9.8	10.7	37.1	XRБ
(4629)	1.46	14.2	15.6	37.3	...

TABLE 21—*Continued*

Source	Model	N_{H} ($\times 10^{22} \text{ cm}^{-2}$)	Γ/kT (Index/keV)	Norm (10^{-5} A)	χ^2/dof or Cstat	Goodness(%) (for Cstat)	F_{abs} ($\times 10^{-15} \text{ erg s}^{-1} \text{ cm}^{-1}$)	F_{unabs} ($\times 10^{-15} \text{ erg s}^{-1} \text{ cm}^{-1}$)	$\log L_X^{unabs}$ (erg s^{-1})	Classification
(4630)	1.11	10.9	11.9	37.2	...
LZB_68 (4628)	apec	0.0436 ^d	0.14 ^{+0.06} _{-0.05}	0.14 ^{+0.56} _{-0.14}	15	89	1.0	1.6	36.3	probable SNR
(4629)	0.92	0.9	1.6	36.3	...
(4630)	0.56	0.6	0.9	36.1	...
LZB_72 (4628)	PL	0.08 ^{+0.12} _{-0.08}	0.06 ^{+0.02} _{-0.01}	0.12 ^{+0.84} _{-0.12}	19.0	58.0	9.5	28.7	37.5	SSS
LZB_75 (2014)	PL	0.0436 ^d	2.88 ^{+1.10} _{-0.92}	0.03 ^{+0.02} _{-0.03}	26.0	91.3	1.1	1.4	36.2	XRB
(4628)	1.19	1.3	1.7	36.3	...
(4629)	0.87	9.2	1.3	36.2	...
(4630)	1.27	1.3	1.8	36.3	...
LZB_76 (2014)	apec	0.48 ^{+0.23} _{-0.19}	0.12 ^{+0.05} _{-0.03}	> 8.4	7.26	68.0	0.8	62	37.9	probable SNR
(4628)	0.63	0.5	39	37.7	...
(4629)	1.35	1.2	83	38.0	...
(4630)	1.11	0.9	68	37.9	...
LZB_78 (2014)	apec	0.0436 ^d	0.70 ^{+0.08} _{-0.11}	0.12 ^{+0.04} _{-0.03}	53.8	84.6	2.7	3.2	36.6	probable SNR
(4628)	0.75	2.0	2.4	36.5	...
(4629)	0.89	2.4	2.8	36.5	...
(4630)	0.88	2.4	2.8	36.5	...
LZB_80 (2014)	apec	0.57 ^{+0.45} _{-0.57}	0.24 ^{+0.55} _{-0.15}	> 0.55	6.27	55.8	0.5	10	37.1	probable SNR ^a
(4628)	1.01	0.5	10	37.1	...
(4629)	3.40	1.6	34	37.6	...
(4630)	1.11	0.5	11	37.1	...
LZB_81 (2014)	apec	0.52 ^{+0.14} _{-0.10}	0.12 ^{+0.04} _{-0.05}	> 6.21	15.1	47	1.0	64	37.9	SNR
(4628)	1.02	1.0	66	37.9	...
(4629)	0.98	0.9	63	37.9	...
(4630)	1.02	1.0	66	37.9	...
LZB_86 (2014)	apec	0.63 ^{+0.23} _{-0.30}	0.18 ^{+0.2} _{-0.09}	> 1.9	6.06	62.3	0.5	29	37.6	probable SNR ^a
(4628)	1.84	0.9	53	37.8	...
(4629)	2.44	1.2	71	37.9	...
(4630)	1.64	0.8	47	37.8	...

NOTE.—For the description of the Columns see Table 20

^aOptically detected SNRs by Matonick et al. (1997)

^bRadio detected SNR by Turner & Ho (1994)

^cRadio detected SNR by Eck et al. (2002)

TABLE 22
SPECTRAL FITTING RESULTS OF THE POINT-SOURCES IN NGC 5204

Source	Model	N_H ($\times 10^{22} \text{ cm}^{-2}$)	Γ/kT (Index/keV)	Norm (10^{-5} A)	χ^2/dof or Cstat	Goodness% (for Cstat)	F_{abs} ($\times 10^{-15} \text{ erg s}^{-1} \text{ cm}^{-1}$)	F_{unabs} ($\times 10^{-15} \text{ erg s}^{-1} \text{ cm}^{-1}$)	$\log L_X^{unabs}$ (erg s^{-1})	Classification
chi-square statistics										
LZB_10 (2028)	PL	$0.16^{+0.01}_{-0.01}$	$2.8^{+0.05}_{-0.04}$	$79.7^{+3.02}_{-3.04}$	1635.6/1069	...	1839	3937	40.0	ULX, XRB
(2029)	0.38	696.8	1492	39.6	...
(3933)	0.58	1064	2278	39.8	...
(3934)	0.28	521.1	1116	39.5	...
(3935)	0.35	651.1	1394	39.6	...
(3936)	1.29	2382	5101	40.2	...
(3937)	1.24	2286	4894	40.1	...
(3938)	0.28	507	1085	39.5	...
(3939)	0.26	487.4	1044	39.5	...
(3940)	0.79	1452	3109	39.9	...
(3941)	1.24	2286	4894	40.1	...
(3942)	0.70	1292	2766	39.9	...
(3943)	1.11	2049	4388	40.1	...
LZB_11 (3941)	PL+apec	$0.01^{+1.04}_{-0.01}$	$\Gamma = 1.20^{+1.17}_{-0.47}$	$1.46^{+1.12}_{-0.48}$	5.79/9	...	179.2	181.9	38.7	XRB
...	kT > 0.8	$0.30^{+6.86}_{-0.30}$
(3942)	1.12	201.6	204.6	38.8	...
(3943)	1.07	191.4	194.3	38.7	...
chi-square statistics										
LZB_8 (3933)	PL	$0.13^{+0.14}_{-0.12}$	$\Gamma = 3.1^{+0.85}_{-0.73}$	$0.41^{+0.27}_{-0.16}$	41.3	5.0	9.7	21.8	37.8	XRB

NOTE.—For the description of the Columns see Table 20

TABLE 23
COMPOSITE SNR/XRB SOURCES

Galaxy	Source ID	apec luminosity ($\times 10^{37}$ erg s $^{-1}$)	PL luminosity ($\times 10^{37}$ erg s $^{-1}$)	Total luminosity ($\times 10^{37}$ erg s $^{-1}$)
NGC 2403	93	—	2.4 (100%)	2.4
NGC 2403	99	2.6 (14%)	16.1 (86%)	18.7
NGC 2403	104	—	92.1 (100%)	92.1
NGC 4214	26	—	10.4 (100%)	10.4

*The numbers in parenthesis indicate the contribution of the luminosity of each component to the total absorption-corrected luminosity. The three X-ray SNRs in NGC 2403 are optically known SNRs while the one in NGC 4214 is associated with a radio SNR/HII source.

TABLE 24
NUMBER OF THE SNRS IN THE MCs AND M33

Galaxy	L_{FIR} ($\times 10^{42}$ erg s $^{-1}$)	Observed SNRs	Rescaled Number of SNRs ($\alpha = -0.5$)	Rescaled Number of SNRs ($\alpha = -1$)
Luminosity distribution of Ghavamian et al. (2005)				
LMC	1.96	31.6	4.5	...
SMC	0.29	8.9	1.3	...
Luminosity distribution of Haberl & Pietsch (2001)				
M33	2.86	9.1	2.6	0.8

NOTE.—The LMC, SMC and M33 FIR luminosities correspond to the 42-122 μ m band and are adopted from Rice et al. (1988). The numbers of the observed SNRs are down to the detection limit of each respective study: for LMC-SMC is 10^{35} erg s $^{-1}$ and for M33 is 8.5×10^{35} erg s $^{-1}$. The observed numbers of the MC SNRs are rescaled to the numbers of SNRs down to our limiting luminosity of 5×10^{36} erg s $^{-1}$ while the observed M33 SNRs are rescaled to the limiting luminosity of Pannuti et al. 2007 (10^{37} erg s $^{-1}$).

TABLE 25
EXPECTED NUMBER OF SNRS (ASSUMING AN MC XLF)

Galaxy	L_{FIR} ($\times 10^{42}$ erg s $^{-1}$)	$(\frac{SNR}{L_{FIR}})_{MC}$ ($\times 10^{-42}$ SNR / (erg s $^{-1}$))	Expected Number of SNRs	Observed SNRs
NGC 3077	0.94	3.38	3.2	5
NGC 4449	4.10	3.38	13.8	3
NGC 4395	0.24	3.38	0.8	1
NGC 4214	2.52	3.38	8.5	5
NGC 5204	0.39	3.38	1.3	0
NGC 2403	4.33	3.38	14.6	8

NOTE.—Column 1: Galaxy ID, Column 2: The 42-122 μ m FIR luminosities of the galaxies based on integrated flux measurements with IRAS in the 60 and 100 μ m bands (Ho et al. 1997), using the calibration of Rice et al. (1988) and the distances in Table 1. Column 3: The average number of MC SNRs (down to 5×10^{36} erg s $^{-1}$) per unit FIR luminosity; see §5.3.2 for details, Column 4: The expected number of SNRs for the galaxies in our sample, derived by rescaling the number of the MC SNRs, Column 5: The observed SNRs for each galaxy down to our detection limit of 5×10^{36} erg s $^{-1}$.

TABLE 26
 EXPECTED NUMBER OF SNRS IN SPIRAL GALAXIES (ASSUMING AN M33-LIKE XLF)

Galaxy	L_{FIR}	$(\frac{SNR}{L_{FIR}})_{M33}$	Expected Number of SNRs	$(\frac{SNR}{L_{FIR}})_{M33}$	Expected Number of SNRs	Observed SNRs
	$(\times 10^{42} \text{ erg s}^{-1})$	$(\times 10^{-42} \text{ SNR} / (\text{erg s}^{-1}))$		$(\times 10^{-42} \text{ SNR} / (\text{erg s}^{-1}))$		
		$(\alpha = -0.5)$	$(\alpha = -0.5)$	$(\alpha = -1)$	$(\alpha = -1)$	
NGC 2403	4.33	0.93	4.0	0.27	1.2	3
M 101	37.2	0.93	34.6	0.27	10.0	7
NGC 6946	36.0	0.93	33.5	0.27	9.7	6
NGC 4736	8.20	0.93	7.6	0.27	2.2	5

NOTE.—Column 1: Galaxy ID, Column 2: The 42-122 μm FIR luminosities of the galaxies are based on integrated flux measurements with IRAS in the 60 and 100 μm bands (Ho et al. 1997) using the calibration of Rice et al. (1988) and the distances from Pannuti et al. (2007), Column 3: Number of M33 SNRs per unit FIR luminosity, down to a limiting luminosity of $10^{37} \text{ erg s}^{-1}$ (Pannuti et al. 2007) and assuming a cumulative slope of - 0.5, Column 4: The expected number of SNRs for $\alpha = -0.5$, estimated by rescaling the M33 XLF by the FIR luminosity of each galaxy (see §5.4 for details), Column 5: Number of M33 SNRs per unit FIR luminosity, down to a limiting luminosity of $10^{37} \text{ erg s}^{-1}$ (Pannuti et al. 2007) and assuming a cumulative slope of - 1, Column 6: Same as Column 4 but for a cumulative slope of $\alpha = -1$, Column 7: Observed SNRs from the sample of galaxies of Pannuti et al. (2007) (down to $10^{37} \text{ erg s}^{-1}$).

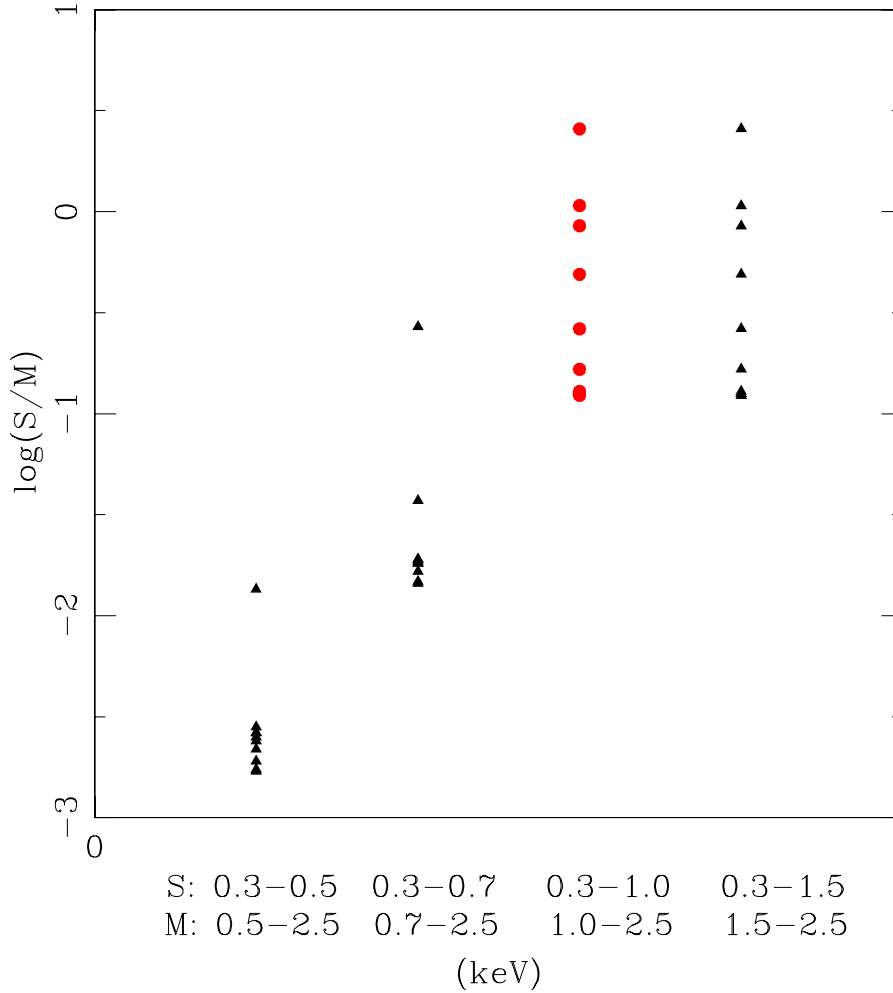


Fig. 1.— Soft/Medium color distribution for different choices of the soft and medium bands. The abscissa shows the different selections for the two bands, while different points show the S/M color which correspond to different choices of temperature (0.25 - 2.0 keV from the bottom towards the top of each data set). The maximum discrimination of the S/M color distribution is seen for the last two energy band choices ($S_3 - M_3$ and $S_4 - M_4$). These energy band selections can allow us distinguish emission lines coming from low temperature thermal emitting gas or harder emission from hotter thermal continuum. The circles denote the S/M color distribution of the two bands that were used by this study (S: 0.3 - 1.0 keV and M: 1.0 - 2.5 keV).

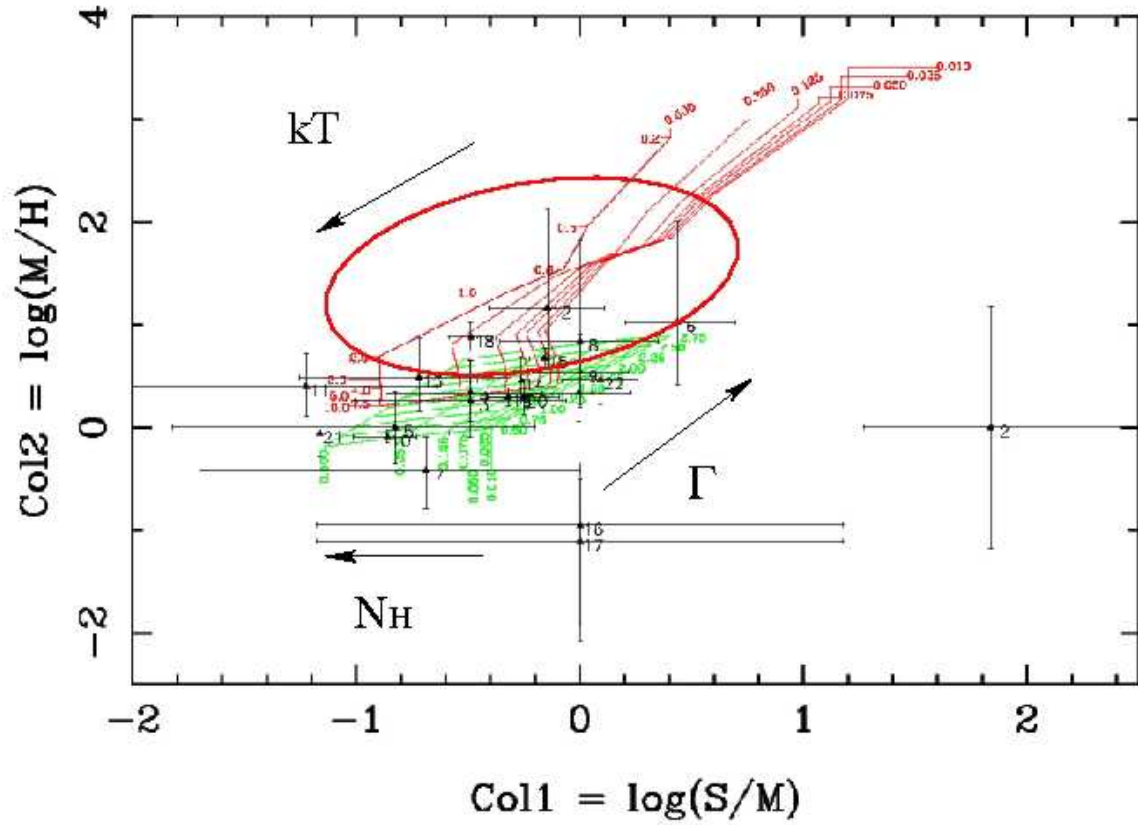


Fig. 2.— Color-color diagram of the detected X-ray sources in NGC 3077. We overplot grids for thermal (red) and power-law (green) models for different values of temperature (kT), absorbing HI column density (N_H) and photon index Γ , calculated for the effective area at the reference point (see §3.3). Sources that appear to have temperatures below 2 keV and mainly lie on the thermal grid (red locus of SNRs) are potential SNRs.[See the electronic edition for a color version of this figure.]

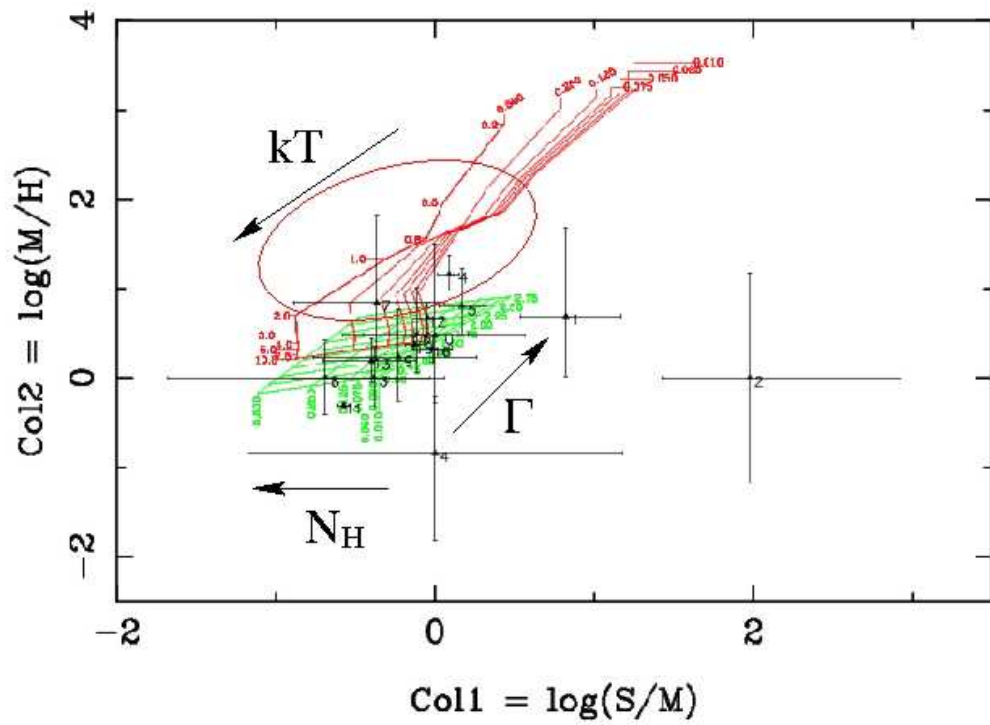


Fig. 3.— Same as Fig. 2 for NGC 4395.

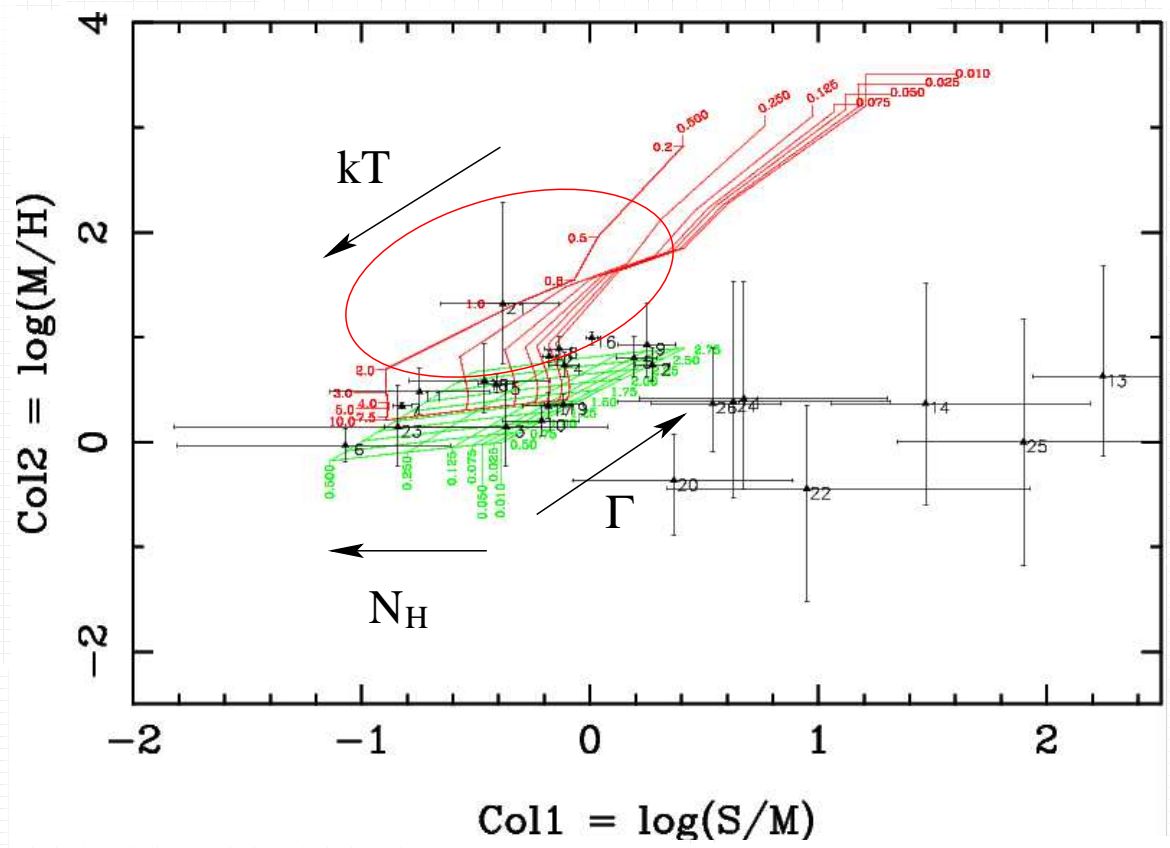


Fig. 4.— Same as Fig. 2 for NGC 4449

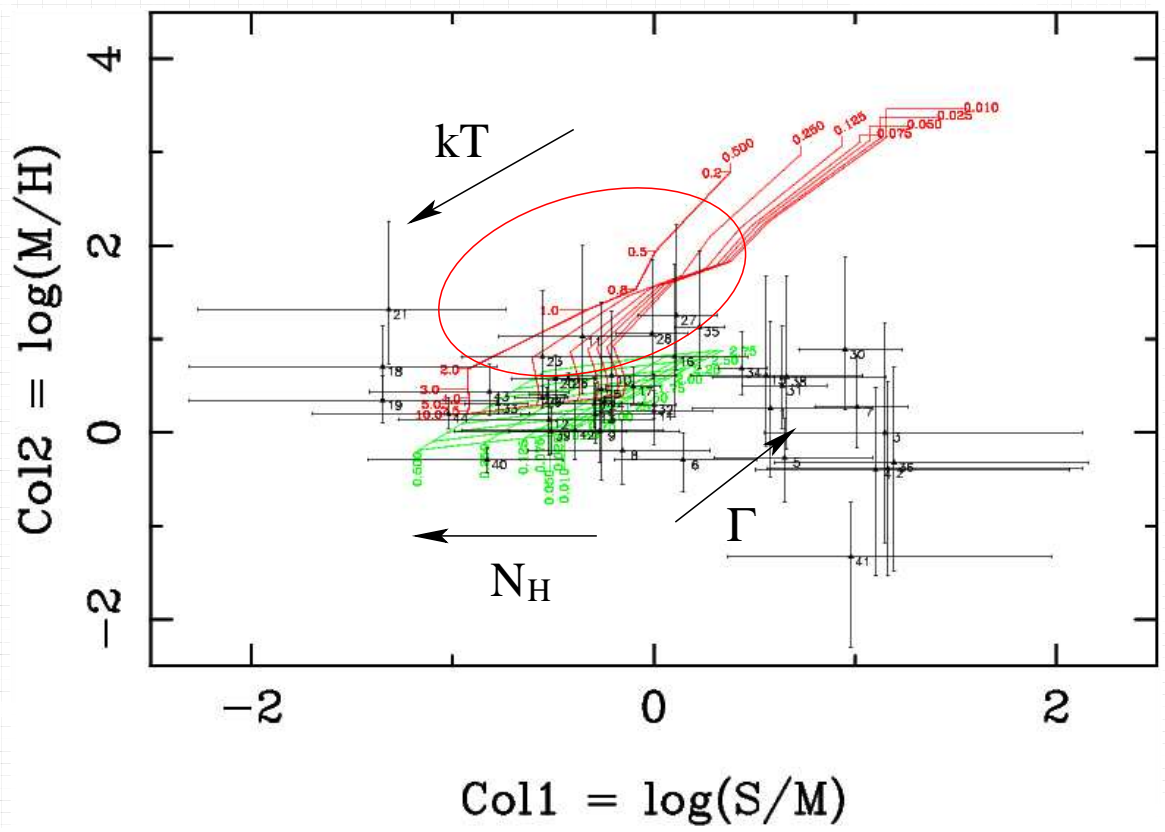


Fig. 5.— Same as Fig. 2 for NGC 4214

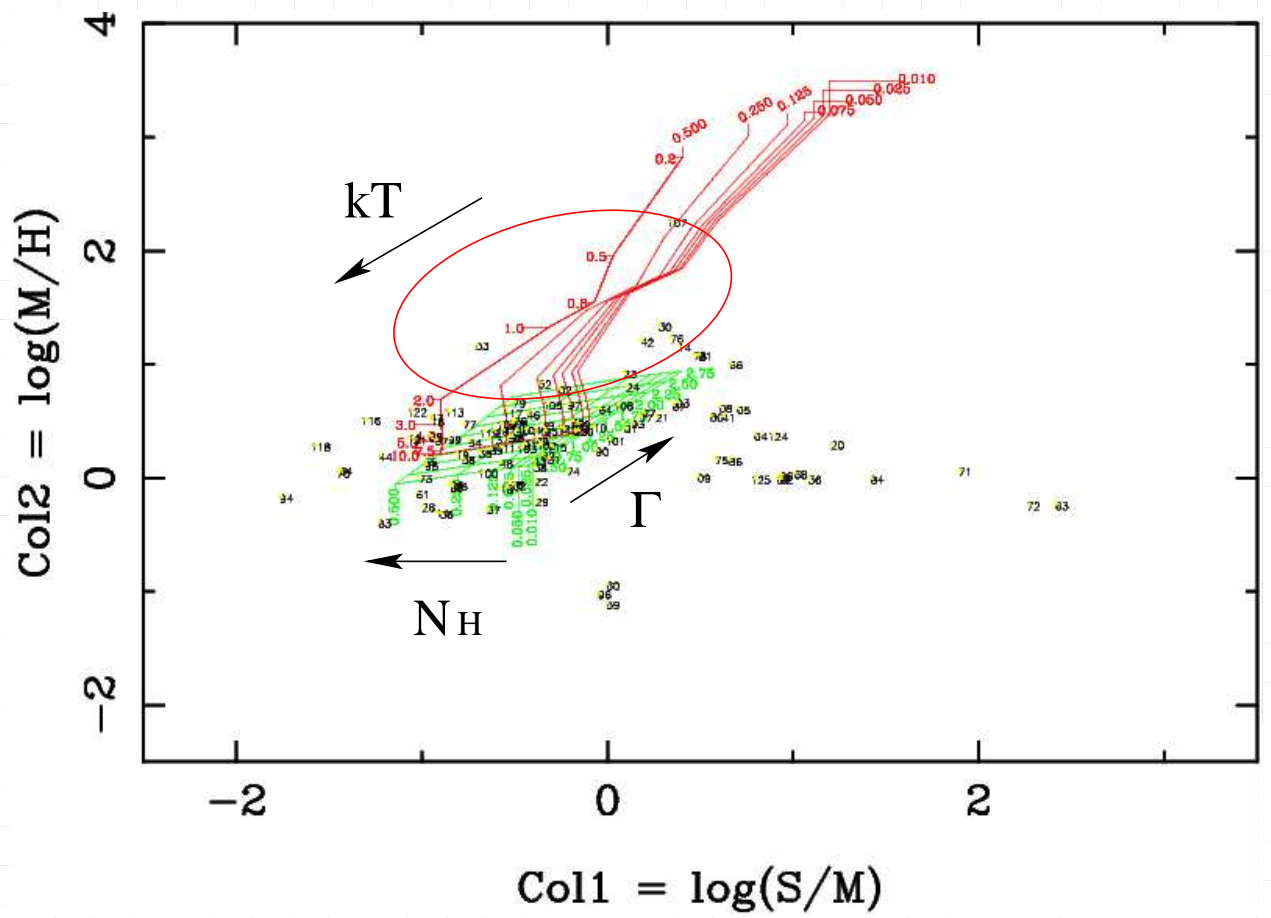


Fig. 6.— Same as Fig. 2 for NGC 2403. Errors were not displayed for clarity.

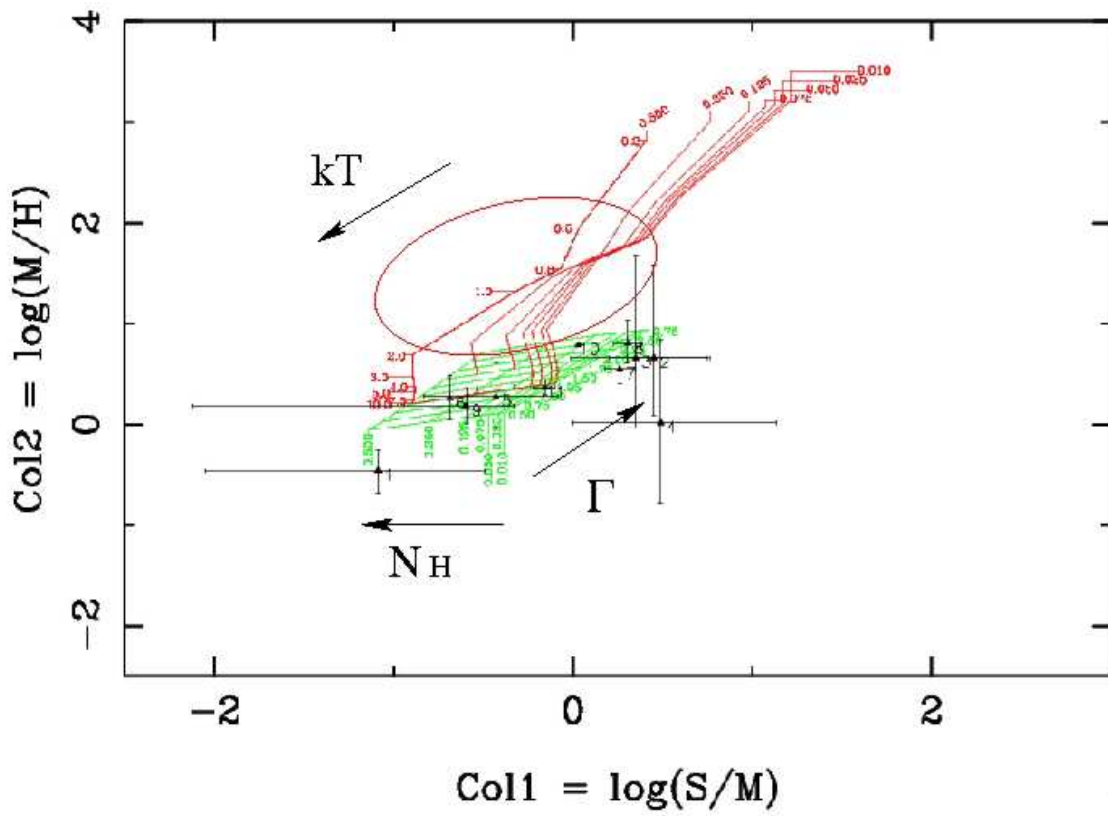


Fig. 7.— Same as Fig. 2 for NGC 5204

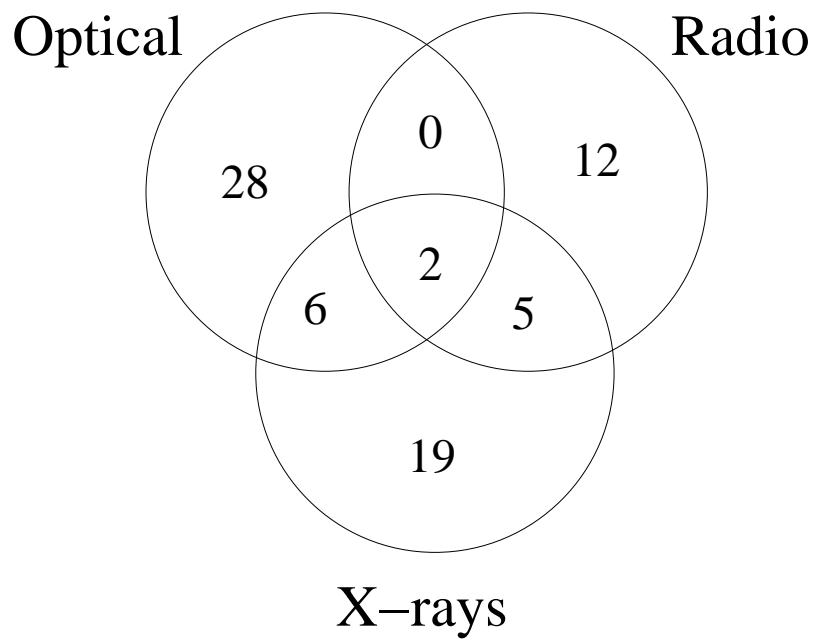


Fig. 8.— Venn diagram for all SNRs detected in our sample of galaxies

NGC 2403

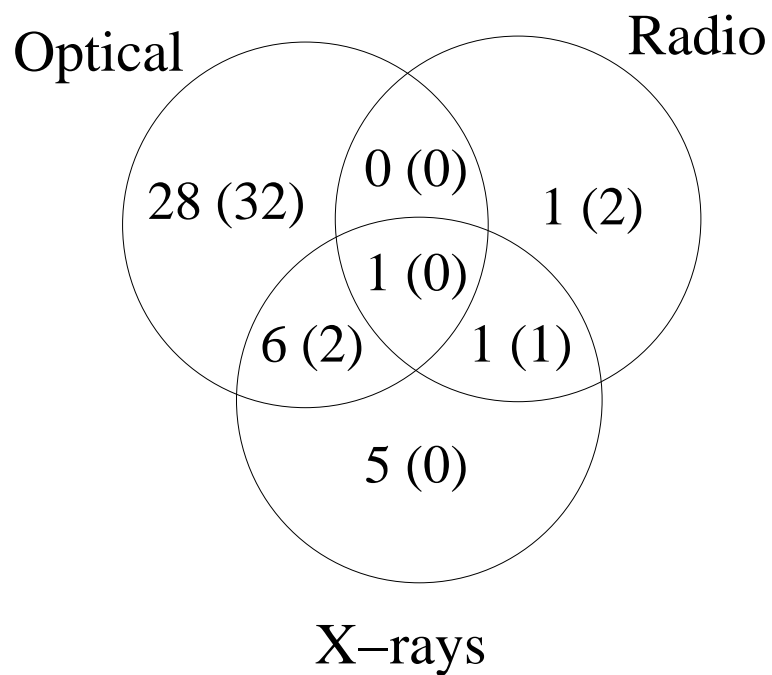


Fig. 9.— Venn diagram for NGC 2403. The numbers in parenthesis refer to the optically/radio SNRs from Pannuti et al. (2007).

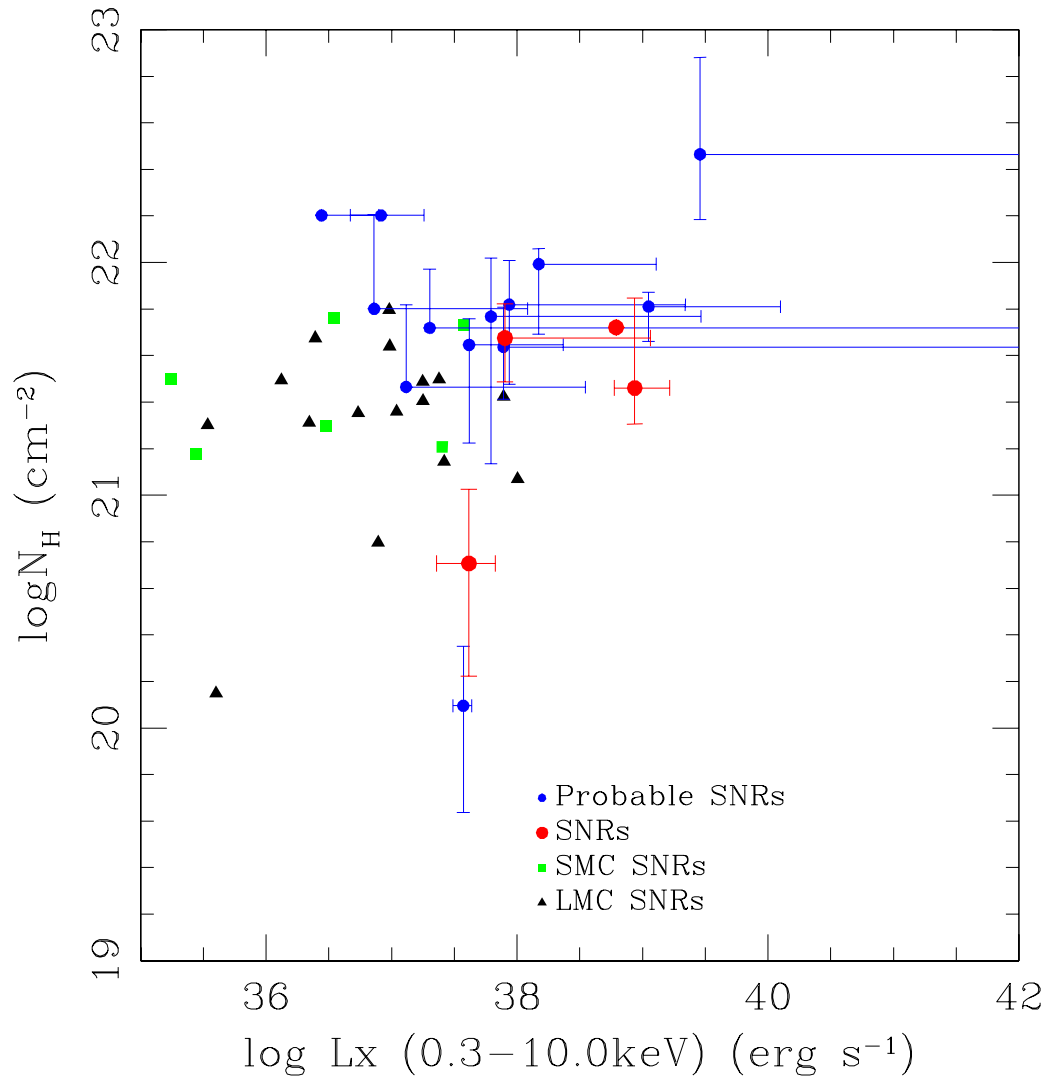


Fig. 10.— The HI column density (corrected for the Galactic column) plotted against the absorption-corrected luminosity. Squares and triangles denote the X-ray SNRs for SMC and LMC respectively while circles represent the X-ray SNRs of this study.

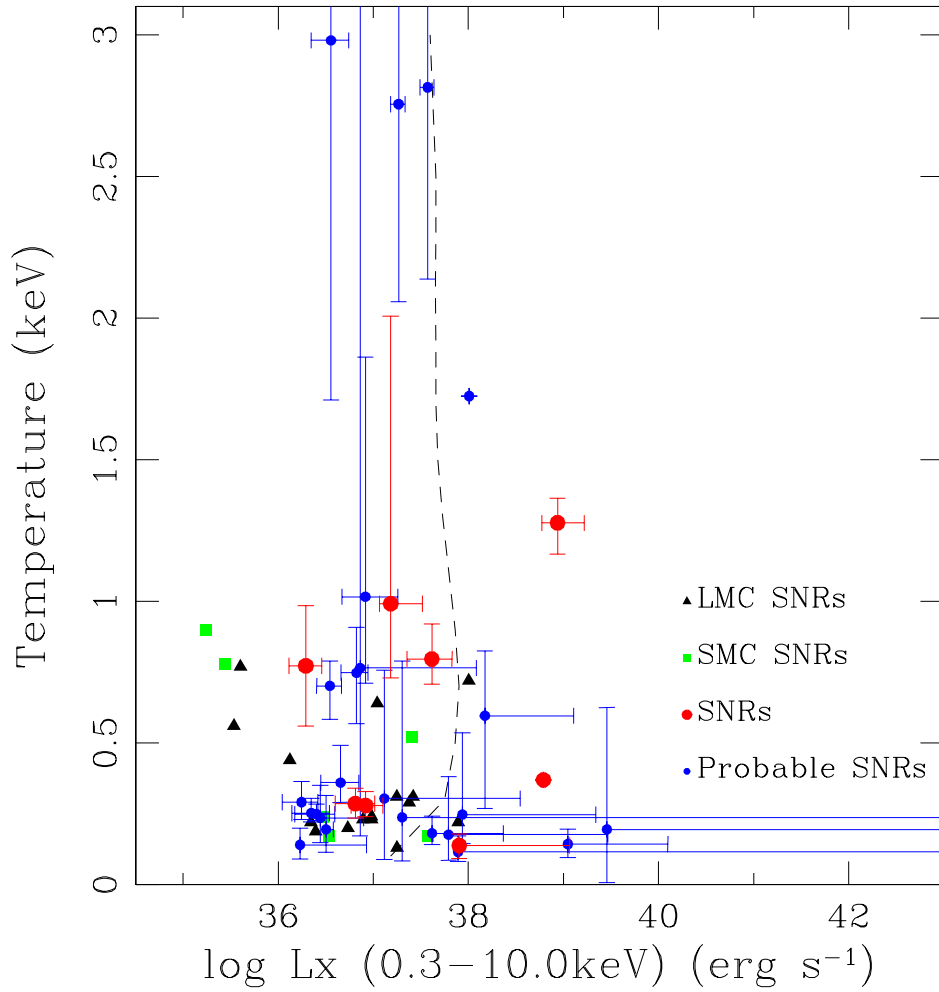


Fig. 11.— Temperature of the X-ray selected SNRs in this study against their absorption-corrected X-ray luminosity. Circles are for the SNRs of this study, squares for the SMC SNRs and triangles for the LMC SNRs. The dashed line shows the expected relation between temperature and luminosity for a thermal source at a distance of 5 Mpc, based on an apc model with a fixed emission measure (EM).

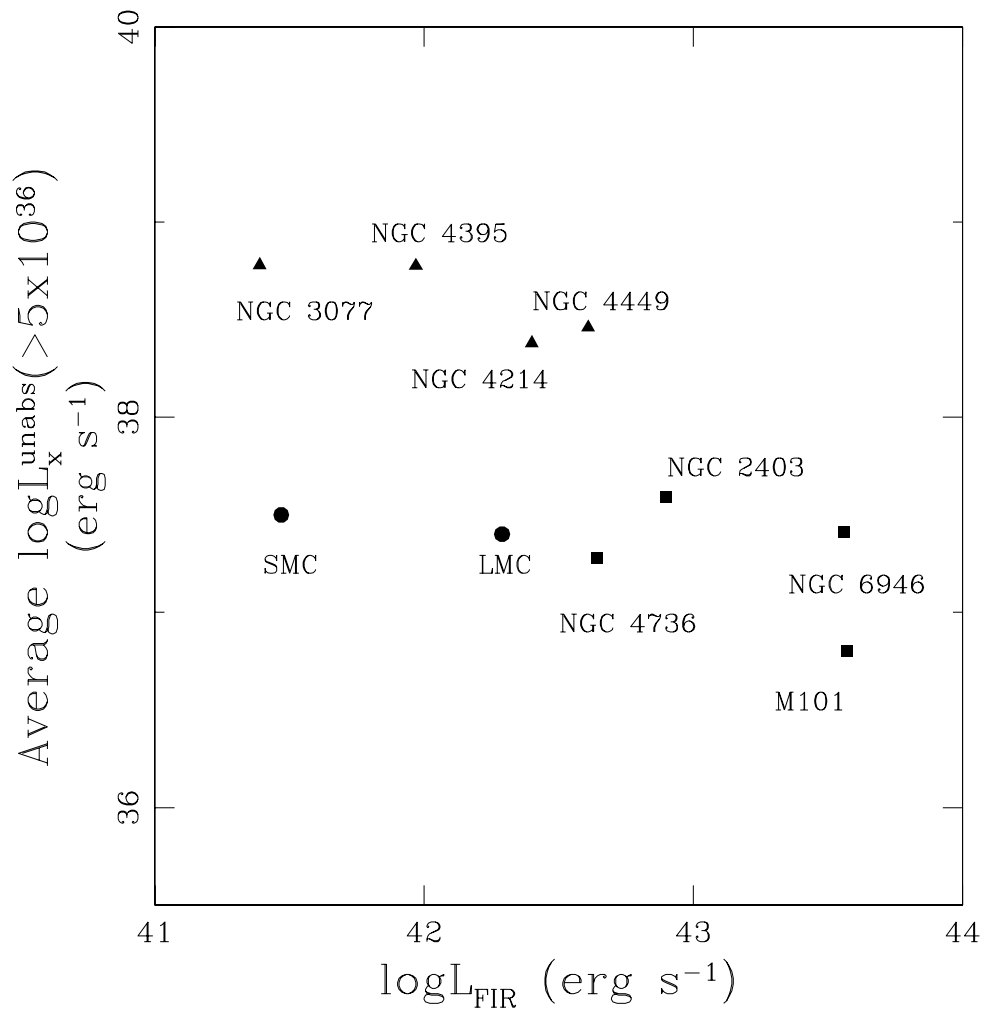


Fig. 12.— The average absorption-corrected X-ray luminosity in the 0.3 - 10 keV band for the SNRs in our sample. We only include objects above the completeness limit of this study (5×10^{36} erg s $^{-1}$). Squares and triangles represent spiral and irregular galaxies respectively while circles correspond to the Magellanic Clouds.

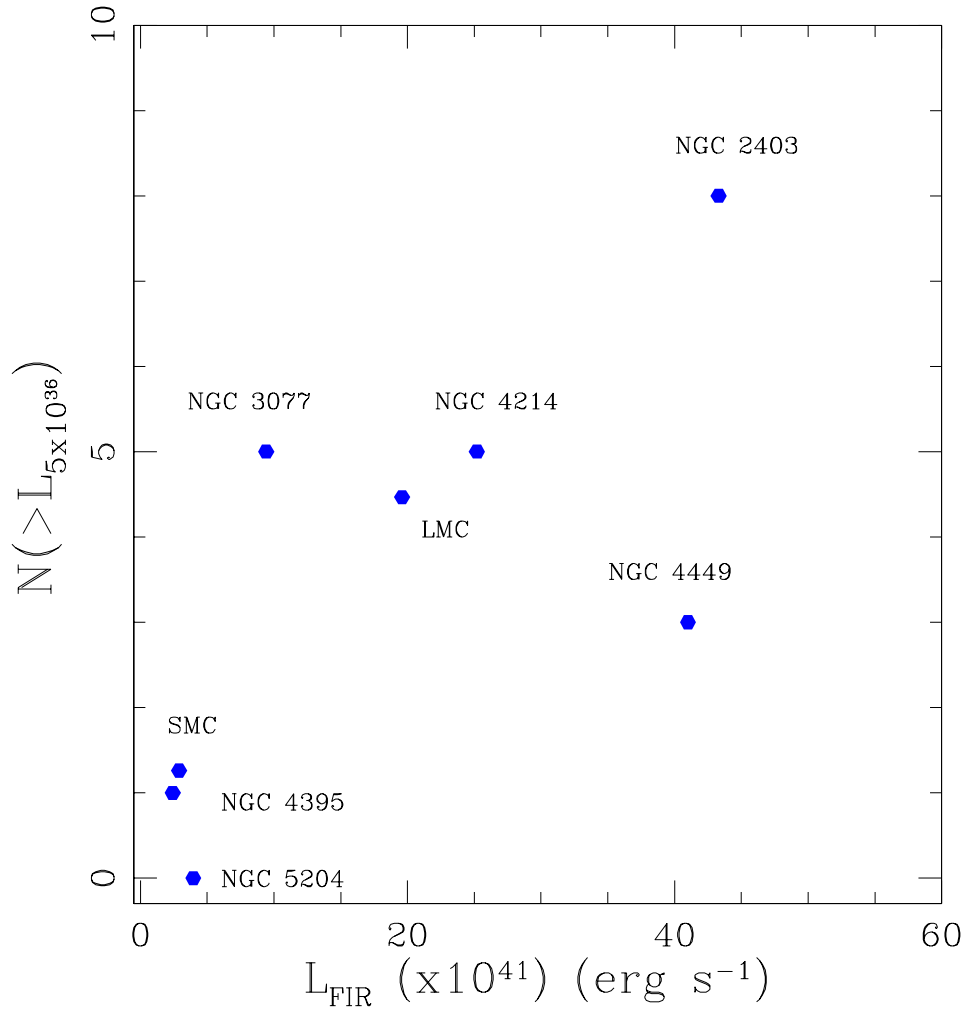


Fig. 13.— Number of SNRs above the completeness limit of this study against the integrated Far Infrared (42–122 μm) luminosity (see text for details).

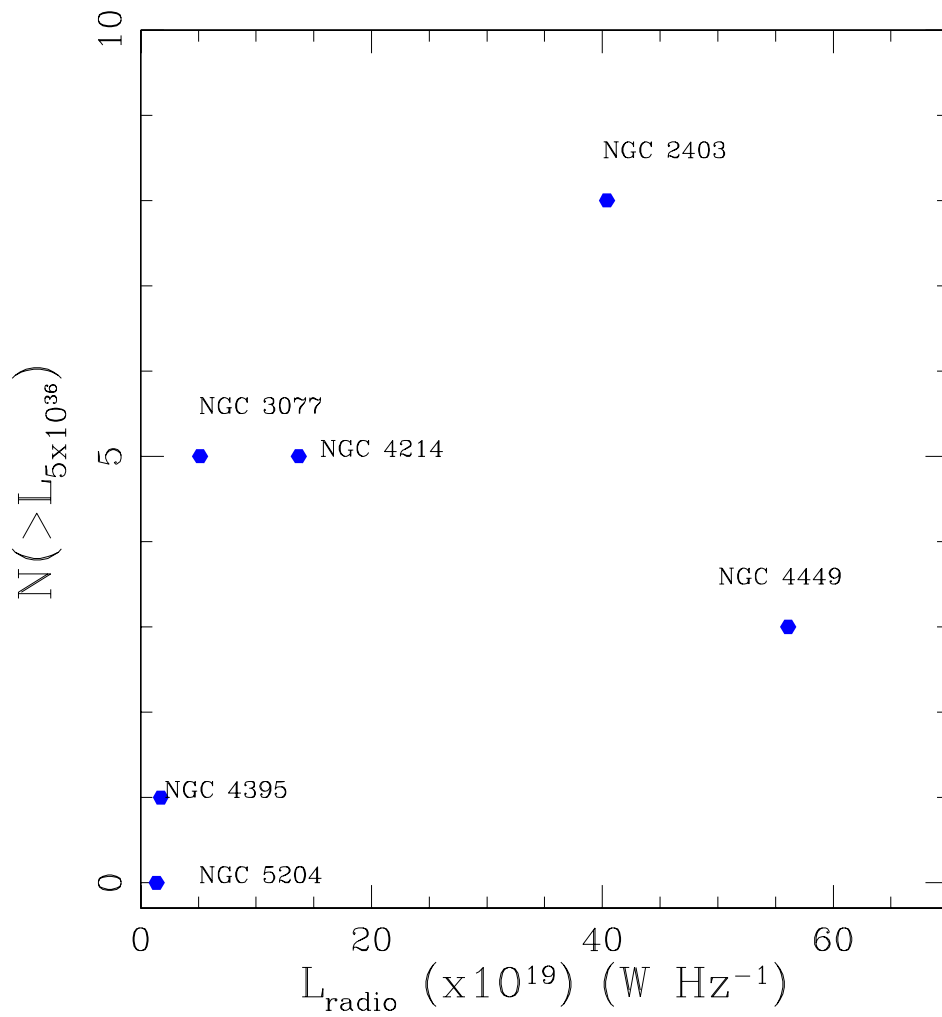


Fig. 14.— Number of SNRs above the completeness limit of this study against the radio luminosity.